A systems-biology approach connects aging mechanisms with Alzheimer's disease pathogenesis

Matthew J Leventhal[1,2,3], Camila A Zanella[4], Byunguk Kang[2,5], Jiajie Peng[6,7], David Gritsch[6,7], Zhixiang Liao[6,7], Hassan Bukhari[4], Tao Wang[6,7,11], Ping-Chieh Pao[8,9], Serwah Danquah[5,10], Joseph Benetatos[2], Ralda Nehme[5,10], Samouil Farhi[5], Li-Huei Tsai[3,8,9], Xianjun Dong[6,7], Clemens R Scherzer[6,7,12], Mel B Feany[4], Ernest Fraenkel[*1,2,3,13]

Corresponding author: Ernest Fraenkel

Summary

Age is the strongest risk factor for developing Alzheimer's disease, the most common neurodegenerative disorder. However, the mechanisms connecting advancing age to neurodegeneration in Alzheimer's disease are incompletely understood. We conducted an unbiased, genome-scale, forward genetic screen for age-associated neurodegeneration in *Drosophila* to identify the underlying biological processes required for maintenance of aging neurons. To connect genetic screen hits to Alzheimer's disease pathways, we measured proteomics, phosphoproteomics, and metabolomics in *Drosophila* models of Alzheimer's disease. We further identified Alzheimer's disease human genetic variants that modify expression in disease-vulnerable neurons. Through multi-omic, multi-species network integration of these data, we identified relationships between screen hits and tau-mediated neurotoxicity. Furthermore, we computationally and experimentally identified relationships between screen hits and DNA damage in *Drosophila* and human iPSC-derived neural progenitor cells. Our work identifies candidate pathways that could be targeted to attenuate the effects of age on neurodegeneration and Alzheimer's disease.

Introduction

[1] MIT Ph.D. Program in Computational and Systems Biology, Cambridge, MA, USA
[2] Department of Biological Engineering, Massachusetts Institute of Technology, Cambridge, MA, USA
[3] Broad Institute of Harvard and MIT, Cambridge, MA, USA
[4] Department of Pathology, Brigham and Women's Hospital and Harvard Medical School, Boston, MA, USA
[5] Spatial Technology Platform, Broad Institute of Harvard and MIT, Cambridge, MA USA
[6] Precision Neurology Program, Brigham and Women's Hospital and Harvard Medical school, Boston, MA, USA
[7] APDA Center for Advanced Parkinson's Disease Research, Brigham and Women's Hospital and Harvard Medical School, Boston, MA, USA
[8] Picower Institute for Learning and Memory, Massachusetts Institute of Technology, Cambridge, Massachusetts, USA
[9] Department of Brain and Cognitive Sciences, Massachusetts Institute of Technology, Cambridge, Massachusetts, USA
[10] Stanley Center for Psychiatric Research, Broad Institute of Harvard and MIT, Cambridge, MA, USA
[11] Present address: School of Computer Science, Northwestern Polytechnical University, Xi'an, China
[12] Present address: Stephen and Denise Adams Center of Yale School of Medicine, CT, USA
[13] Lead contact
[*] Correspondence: fraenkel@mit.edu

Neurodegenerative diseases are characterized by a progressive loss of neurons and pathological protein aggregation. Age is the most important risk factor for these diseases, which can lead to cognitive decline and motor defecits[1]. As the global population ages, there is an increasing imperative to understand and design effective therapies for neurodegenerative disorders. Alzheimer's disease, the most common neurodegenerative disorder, is characterized by pathological aggregation and deposition of extracellular amyloid β plaques and intracellular neurofibrillary tangles comprised of tau protein[2–4]. The presence of amyloid β plaques and tau neurofibrillary tangles precedes neuronal death and cognitive decline[5]. Amyloid β plaques are predominantly made up of 42-amino acid amyloid β oligomers (amyloid $\beta_{1\text{-}42}$), which accumulate due to erroneous cleavage of the amyloid precursor protein (*APP*)[6]. Furthermore, point mutations in the gene microtubule-associated protein tau (*MAPT*) lead to increased tangle formation and neuronal cell death in the neurodegenerative condition frontotemporal dementia, illustrating how tau can contribute to neuronal cell death[7].

While aging is a key risk factor of Alzheimer's disease, it is not clear which aging-related biological processes lead to neurodegeneration and pathophysiological changes in disease[1]. Understanding the biological basis for age-associated neuronal cell death could provide an important new set of therapeutic targets in Alzheimer's disease and related age-dependent neurodegenerative disorders[8]. Previous genome-wide association studies (GWAS), transcriptomic analysis, and quantitative trait locus (QTL) analysis have identified genetic risk factors and associated molecular changes underlying Alzheimer's disease in the brain at bulk and single-neuron resolution[9–16]. However, the mechanisms by which many QTL-associated molecular changes impact neurodegenerative disease pathogenesis remain undefined.

To define mechanisms maintaining neuronal function and viability with advancing age, we performed a neuron-specific, *in vivo* genome-scale RNAi screen in *Drosophila* (Figure 1, Figure 2A). The short lifespan of *Drosophila* makes it possible to assess age-associated effects of gene knockdowns that would be challenging to study in other model organisms[17–19]. *Drosophila* and humans share numerous conserved genetic, cellular, electrophysiological and chemical properties[20]. The fruit fly also exhibits many of the same molecular phenotypes associated with advancing age as humans[18,21–23]. These observations suggest shared mechanisms of age-associated neurodegeneration between humans and *Drosophila*. Our work builds on previous efforts that used genome-scale screens in *Drosophila* to identify regulators of tau-mediated neurotoxicity, as well as other work that identified neuron-essential genes in human induced pluripotent cell-derived neurons[24–27].

To relate the hits from our model organism screen to human disease, we used a multi-omic integration approach to identify the pathways that influence age-associated neurodegeneration. We measured proteomics, phosphoproteomics and metabolomics in transgenic *Drosophila* models of human amyloid β and tau to identify molecular changes associated with Alzheimer's disease toxic proteins (Figure 1). To determine how our neuron-specific RNAi screen and the related model organism data were important in human Alzheimer's disease patients, we generated RNA-sequencing (RNA-seq) data from pyramidal neuron-enriched populations from the temporal cortex using laser-capture microdissection[28–32]

(Figure 1). We were particularly interested in measuring this neuronal cell type and brain region because they are especially vulnerable to the formation of neurofibrillary tangles[29]. We identified fine-mapped expression QTLs (eQTLs) and the eQTL-associated genes (eGenes) in neurons vulnerable to disease pathology to find patterns of gene expression associated with human genetic risk factors of Alzheimer's disease. Next, we integrated these multi-species, multi-omic data with a previously published genome-scale screen for tau-mediated neurotoxicity[24], existing human Alzheimer's disease GWAS hits, proteomics, and metabolomics [10,12,24,33,34] using the Prize-Collecting Steiner Forest algorithm (Figure 1)[35,36]. This approach has been used to identify biological processes in various disease consequences, including Alexander disease, medulloblastoma, Parkinson's disease in *Drosophila*, amyotrophic lateral sclerosis, and an *Appl* model of Alzheimer's disease in *Drosophila*[37–41].

Based on our integrated model, we nominated genes and pathways that contribute to age-associated neurodegeneration in Alzheimer's disease. We experimentally tested the predicted functional effects of knockdown of proposed targets in flies and in human induced pluripotent stem cells. Specifically, we demonstrate that the human Alzheimer's disease genetic risk factor *MEPCE* and neurodegeneration screen hit *HNRNPA2B1* regulate tau-mediated neurotoxicity. Furthermore, we show in flies and iPSC-derived neural progenitor cells that *NOTCH1* and *CSNK2A1* regulate the DNA damage response, suggesting pathways through which these genes enhance age-associated neurodegeneration.

Results

A genome-scale, forward genetic screen identifies regulators of age-associated neurodegeneration in Drosophila

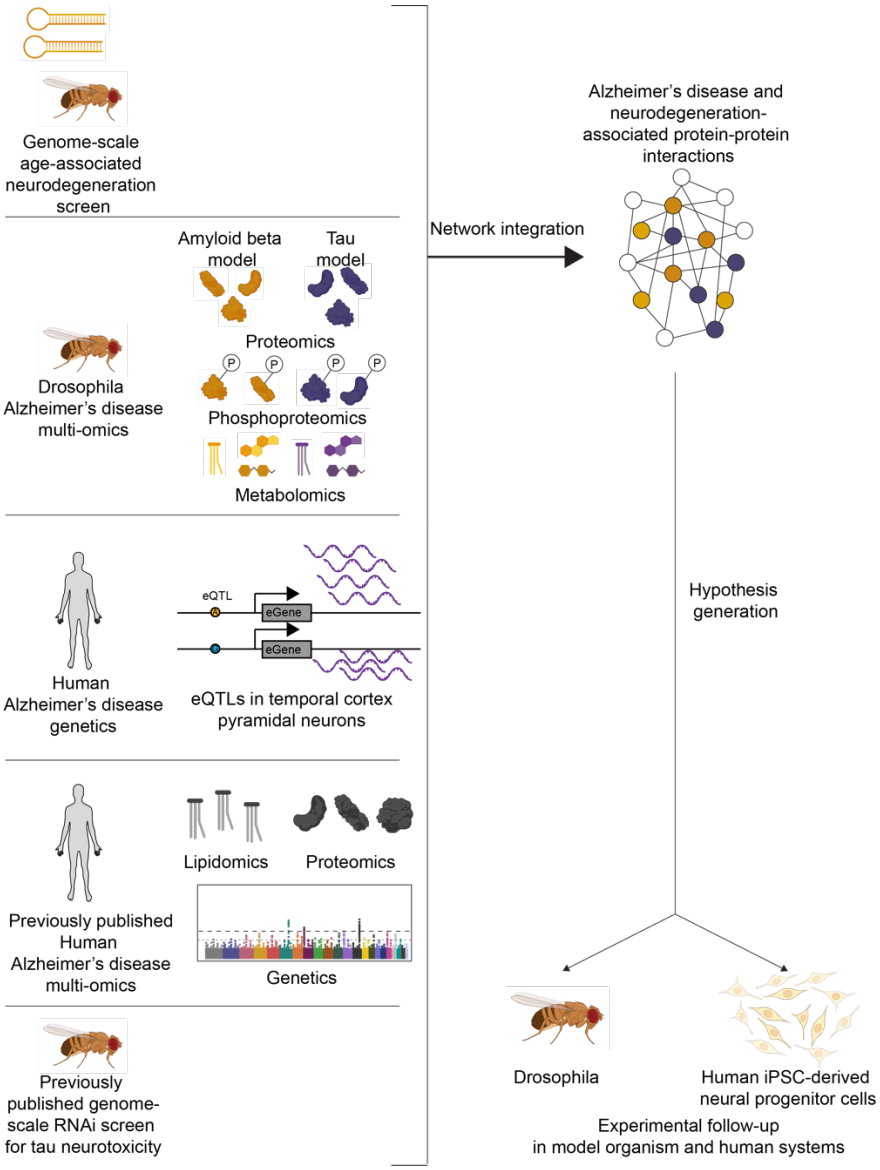

Figure 1. Overview of analytical framework in this study for multi-omic integration to understand the biological processes underlying neurodegeneration. We performed a forward genetic screen for age-associated neurodegeneration in *Drosophila*. We measured proteomics, phosphoproteomics and metabolomics in amyloid β (gold) and tau (purple) models of Alzheimer's disease and performed an eQTL meta-analysis of previous Alzheimer's disease studies. We used a network integration model to integrate these new data with previously published human proteomics, human genetics, human lipidomics, and *Drosophila* modifiers of tau-mediated neurotoxicity. We tested hypotheses generated from this network model in *Drosophila* and human iPSC-derived neural progenitor cells. Icons created with Biorender.com.

To identify the genes required to maintain the viability of aging neurons *in vivo* we performed a genome-scale, forward genetic screen in *Drosophila* (Figure 2A). Age-associated neurodegeneration is a hallmark of human Alzheimer's disease and can be experimentally

assessed in a model organism with a short lifespan like *Drosophila*[2,17–19]. We used a transgenic RNAi screen to knock down 5,261 *Drosophila melanogaster* genes in neurons, aged the flies for 30 days, and assessed brain integrity using hematoxylin and eosin-stained tissue sections (Figure 2A). Neurodegeneration is frequently accompanied by neuropil vacuolation in flies and in human neurodegenerative disease[42–45]. From this screen, we identified 198 genes that promoted age-associated neurodegeneration in *Drosophila* after knockdown (Table 1 and referred to below as "screen hits"). A simple pathway enrichment approach showed that the hits were overrepresented by genes involved in neuronal morphogenesis, development, cell death, and memory in *Drosophila* (Table S1, Benjamini-Hochberg FDR-adjusted p-value<0.1).

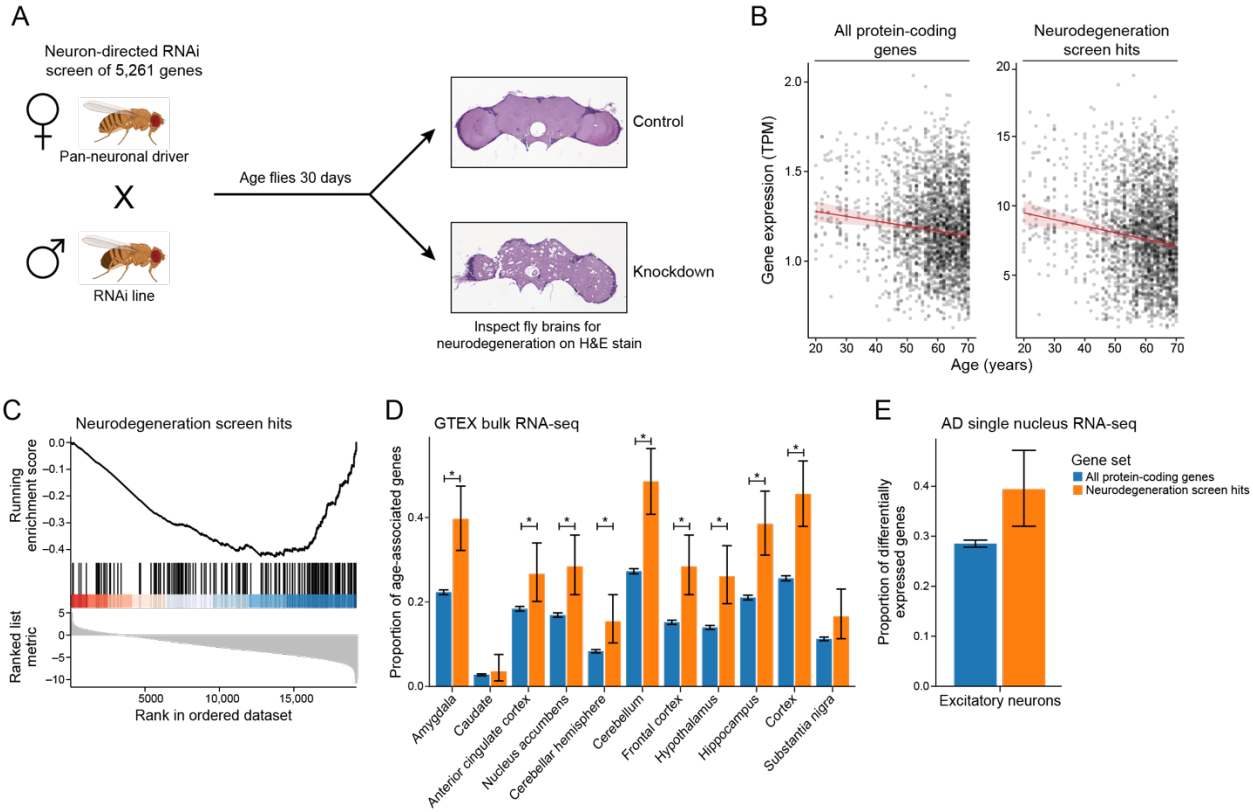

Figure 2. A) Schematic of the genetic screen for age-associated neurodegeneration. Upon neuron-specific RNAi knockdown, neurodegeneration is assayed on H&E-stained brain sections and is frequently vacuolar. Example control and knockdown images are shown. *Drosophila* cartoons were created with Biorender.com. B) Geometric mean expression in transcripts per million (TPM) of age-associated neurodegeneration genes (neurodegeneration genes) and all protein-coding genes in the Genotype-Tissue Expression (GTEx) shows that the expression of neurodegeneration screen hits declines with age in human brain tissues. Regression lines indicate the relationship between age and TPM with a 95% confidence interval (standard error of the mean). The mixed effects regression analysis controlled for post-mortem interval, sex, ethnicity, and tissue of origin. Y axes of the left and right plots are on different scales. C) Gene set enrichment plot showing that the set of age-associated neurodegeneration genes has reduced expression with respect to age. Vertical lines indicate rank of neurodegeneration screen hits by their association between gene expression and age determined by mixed-effects

regression analysis coefficients. D) Proportion of genes that have significant associations between gene expression and age relative to the set of all protein-coding genes (blue) or the set of age-associated neurodegeneration genes (orange). Error bars indicate 95% binomial confidence intervals of the estimated proportion of genes with a significant association with age. Asterisk indicates tissues with an FDR-adjusted one-tailed hypergeometric test p-value less than 0.01. E) Proportion of protein-coding genes (blue) and age-associated neurodegeneration genes (orange) that are differentially expressed between Alzheimer's disease (AD) and control in excitatory neurons in single-nucleus RNA-seq. Error bars indicate 95% binomial confidence intervals.

Drosophila gene	human gene	function
Adf1		
Adh	HPGD	
AlCR2	SSTR2	Somatostatin receptor type 2
alien	COPS2	COP9 signalosome complex subunit 2
AP-1gamma	AP1G1	AP-1 complex subunit gamma-1
AP-50	AP2M1	Clathrin coat assembly protein AP50
Apc	APC	Adenomatous polyposis coli protein
Aph-4	ALPP	Alkaline phosphatase
aPKC	PRKCI	Atypical protein kinase C-lambda/iota
Appl	APP	Amyloid precursor protein
arm	CTNNB1	Beta-catenin
Arp8	ACTR8	actin binding
Arpc3A	ARPC3	actin binding
Atg18	WIPI2	WD repeat domain phosphoinositide-interacting protein 2
Atg8a	GABARAP	LC3, autophagy
Atx-1	ATXN1	
barr	NCAPH	non-SMC condensin I complex
bel	DDX3X	ATP-dependent RNA helicase DDX3X
BicD	BICD1	bicaudal D homolog 1
bif		actin binding
burs		neuropeptide, not conserved
Cad99C	PCDH15	Protocadherin-15
CAP-D2	NCAPD2	Condensin complex subunit 1
cdi	TESK2	
cdm	IPO13	Karyopherin-13
CG10200		
CG10738	NPR1	
CG10864	KCNK18	K channel
CG11105	NKD1	naked cuticle homolog 1
CG11198	ACACA	acetyl-Coenzyme A carboxylase
CG11723		
CG12455	CACNA2D3	calcium channel, voltage-dependent, alpha 2/delta subunit
CG13253		
CG13779	SHFM1	protease
CG1440	BLMH	bleomycin hydrolase
CG14419		
CG15021		
CG15177	EFCAB1	
CG15658		
CG1908		
CG2116		transcription factor, not conserved
CG30020		transcription factor
CG30203	SPON1	protease inhibitor
CG31105		sodium trnasporter
CG33213		transcription factor
CG33231	SVIL	gelsolin-like, actin binding
CG33673		
CG33967	KIBRA	WW domain-containing protein 1
CG34402		
CG34422	ARID4A	Retinoblastoma-binding protein 1
CG42260	CNGA2	cyclic nucleotide activated channel
CG42534		
CG42573		
CG4596	TMEM169	
CG6044		

CG6498	MAST1	Microtubule-associated serine/threonine-protein kinase 1
CG7023	USP12	
CG7526	LTBP1	TGF-beta1-BP-1
CG7841	C16orf14	
CG8245	TMEM53	Transmembrane protein 53
CG9086	UBR2	E3 ubiquitin-protein ligase UBR2
CG9934	UBE4B	Ubiquitin conjugation factor E4 B
Cha	CHAT	
CheB38a		
Chmp1	Chmp1b	Chmp1b
chn		transcription factor, not conserved
Cklalpha	CSNK1A1	
CkIIalpha	CSNK2A1	
CkIIbeta	CSNK2B	
Clc	CLTB	Clathrin light chain B
Cont	CNTN6	contactin 6
CoRest	RCOR2	REST corepressor 2
CG5037	COX10	cytochrome-c oxidase
crb	CRB1	Crumbs homolog 1
crm	CRAMP1L	chromatin regulation
csw	PTPN11	protein tyrosine phosphatase
ct	CUX1	Protein CASP/transcription factor
cwo	BHLHE41	Class E basic helix-loop-helix protein 41
dco	CSNK1E	Casein kinase I-epsilon
Dl	DLL1	Delta-like protein 1
dm	MYC	Myc
dock	NCK1	NCK adaptor protein 1
ear	MLLT1	Protein ENL
Eb1	MAPRE1	Microtubule-associated protein RP/EB family member 1
Egfr	ERBB3	
Eip75B	NR1D1	nuclear receptor
endoB	SH3GLB2	Endophilin-B2
epsilonCOP	COPE	
exo84	EXOC8	exocyst complex component 8
ey	PAX6	
eya	EYA1	Eyes absent homolog 1
fliI	FLII	flightless-1 homolog
fng	RFNG	Beta-1,3-N-acetylglucosaminyltransferase
fu	STK36	Serine/threonine-protein kinase 36
fz	FZD1	Frizzled-1
Gadd45	GADD45G	
garz	GBF1	BFA-resistant GEF 1
Gbeta76C	GNB3	
Gef26	RAPGEF2	
gish	CSNK1G3	Casein kinase I isoform gamma-3
gl		transcription factor
GluRIIB	GRIK4	
gsb-n	PAX3	
Hem	NCKAP1	Nck-associated protein 1
hep	MAP2K7	MAP kinase
hh	DHH	Desert hedgehog protein
hippo	STK3	
hiw	MYCBP2	E3 ubiquitin-protein ligase MYCBP2
HLH4C	LYL1	Lymphoblastic leukemia-derived sequence 1
HLHm3	HES6	
HLHMgamma	HES2	Transcription factor HES-2
Hnf4	HNF4A	
HP1c	CPX5	HP1
Hrb98DE	HNRNPA2B1	Heterogeneous nuclear ribonucleoprotein
Hsf	HSF1	Hsf
inx2		gap junction
IP3K1	ITPKA	
klar		
Lam	LMNB1	Lamin-B1
lbk	LRIG3	LRR/Ig
Lim3	LHX3	
lin19	CUL1	
Lis-1	PAFAH1B1	Lissencephaly-1
Lkr	TACR3	Neuropeptide Y receptor related
Lmpt	FHL2	
lz	RUNX3	
mago	MAGOHB	RNA binding
mbl	MBNL1	RNA binding
mib1	MIB1	E3 ubiquitin-protein ligase MIB1
Mlc2	MLY2	

mol	DUOXA1	Dual oxidase maturation factor 1
msn	MAP4K4	JNK pathway
msps	CKAP5	
MstProx	TLR7	
Mtch	MTCH2	Mitochondrial carrier homolog 2
mtTFB2	TFB2M	
mxc	NPAT	activates histone transcription during cell cycle
N	NOTCH1	
NaCP60E	SCN8A	
net	ATOH8	transcription factor, atonal related
neur	NEURL1B	E3 ubiquitin-protein ligase NEURL3
ninaE	OPN4	
Nplp3		
nuf	RAB11FIP4	Rab11 family-interacting protein 4
nvy	CBFA2T3	
Obp44a		
okr	RAD54L	RAD54-like
Or98b		
osk		
Pis	CDIPT	Phosphatidylinositol synthase
pncr002:3R		
Porin2	VDAC3	
Pp4-19C	PPP4C	Serine/threonine-protein phosphatase 4
ppk21	ASIC3	
Psn	PSEN1	
ptc	PTCH1	
Rab9	RAB9B	
Rala	RALA	Ras-related protein Ral-A
Ras85D	HRAS	HRas
rdgB	PITPNM2	
RhoGEF2	ARHGEF12	
RhoGEF3	SPATA13	
ro	GBX2	transcription factors
rok	ROCK1	Rho-associated protein kinase 1
Rph	RPH3A	Rabphilin-3A
rpk	ASIC2	Na channel
Rya-r44F	RYR2	Ryanodine receptor 2
sals	SCAF1	actin binding
santa-maria	CD36	scavenger receptor
scrib	LRRC1	
sec6	EXOC3	
sev	ROS1	
Sfmbt	MBTD1	MBT domain-containing protein 1
shg	CDH20	cadherin
snRNP-U1	SNRPC	
Sod	SOD1	
spi	TRADD	
Stam	STAM	
Stat92E	STAT5B	
sty	SPRY3	EGFR signaling
Syt1	SYT1	
Syt14	SYT14	
Syt4	SYT4	
Tango14	NUS1	Nogo-B receptor Precursor
Tao-1	TAOK1	Serine/threonine-protein kinase TAO1
Tim8	TIMM8B	
Tm2	TPM3	Tropomyosin alpha-3 chain
TrpA1	TRPA1	
trr	MLL3	Histone-lysine N-methyltransferase MLL3
usnp	SNAP29	Synaptosomal-associated protein 29
vap	RASA1	Ras GTPase-activating protein 1
Vap-33-1	VAPB	VAMP-B
Vps36	VPS36	
Vps37A	VPS37A	ESCRT
WASp	WASL	N-WASP
wdb	PPP2R5E	PP2A, B subunit
woc	ZMYM4	zinc finger, MYM-type 4
wtrw	TRPV1	calcium channel

Table 1. Hits from the age-associated neurodegeneration screen: List of *Drosophila* genes and human orthologs that were hits from the screen for age-associated neurodegeneration.

We wanted to know if these screen hits were associated with human aging. We analyzed RNA-seq data from 2642 human post-mortem brain tissues from the Genotype-Tissue Expression

(GTEx) project and found that the mean expression of the screen hits in human brains was negatively associated with chronological age (Figure 2B, right). There was a stronger negative association between average gene expression and age for the neurodegeneration screen hits than the association between average expression of all protein-coding genes and age (Figure 2B, left). We subsequently ranked all genes by the regression coefficients measuring the relationship between gene expression and age. We performed Gene Set Enrichment Analysis on this ranked list to identify which pathways had significant changes in gene expression with respect to age. Our analysis showed a negative association between the expression of screen hits and age (Figure 2C, Benjamini-Hochberg FDR-adjusted p-value<0.1). To assess the robustness of our results, we performed permutation tests by randomly shuffling the patient ages. Not a single permutation out of 10,000 iterations had a more significant association between age and gene expression of the screen hits, suggesting that this result is specific to chronological age in humans.

Next, we examined expression of screen hits with respect to age across regions of the human brain (Figure 2D). Tissues enriched in age-associated changes of the screen hits include Alzheimer's disease-vulnerable regions such as the hippocampus and the frontal cortex (Figure 2D, hypergeometric test Benjamini-Hochberg FDR-adjusted p-value<0.1). In many cases, the same genes showed significant age-associated changes in expression in several tissues (Figure S1, mixed effect model Benjamini-Hochberg FDR-adjusted p-value<0.1, absolute value of regression coefficient>0.1). We observed that the Alzheimer's disease-vulnerable tissues clustered together and with the Parkinson's disease-vulnerable substantia nigra by hierarchical clustering (Figure S1). These human results suggest that the hits from our screen are associated with human aging in multiple regions of the brain, some of which are affected by common neurodegenerative diseases.

To examine cellular specificity, we analyzed the single nuclear RNA-seq data of excitatory neurons from a previously published single-nucleus RNA-seq study[46]. We observed that the average expression of screen hits was lower in Alzheimer's disease-associated excitatory neurons than in excitatory neurons from healthy controls (Figure S2). We also found that the genes differentially expressed in Alzheimer's disease-associated excitatory neurons in this dataset were enriched for neurodegeneration screen hits (Figure 2E, Benjamini-Hochberg FDR-adjusted p-value<0.1). These results show that the gene expression of the screen hits declines with respect to age in human brain tissues and human Alzheimer's disease excitatory neurons, suggesting their importance in human disease and aging.

Human genetic risk factors enriched in disease-associated neurons complement results from the neurodegeneration screen

We wanted to examine how the hits from our neuron-specific RNAi screen in *Drosophila* relate to genetic causes of Alzheimer's disease in human neurons. To that end, we used laser-capture microdissection to obtain pyramidal neurons from the human temporal cortex of 75 individuals (Figure 3A). We then performed RNA-seq and eQTL analysis on these samples (Figure 3A, TCPY in Table S2). We were interested in pyramidal neurons of the temporal cortex because this

neuronal subtype is vulnerable to neurofibrillary tangle-mediated neurotoxicity in Alzheimer's disease[29]. We first performed an eQTL meta-analysis across 7 different bulk RNA-seq and genomics studies in post-mortem brains (Tables S2, S3, Methods). The results from this meta-analysis were then forwarded to the eQTL analysis in the newly collected temporal cortex pyramidal neuron RNA-seq data to see which brain eQTLs were enriched in Alzheimer's disease-vulnerable neurons. We found *cis*-regulatory effects in the pyramidal neuron-enriched transcriptomes for 12 eGenes (Table 2). The enriched genes included *C4A*, *EPHX2*, *PRSS36*, and multiple MHC class II genes (Table 2). Expression of the eGenes was correlated with several known biological processes previously associated with Alzheimer's disease such as insulin signaling, protein folding and lipid metabolism[46–58] (Figure S3). We incorporated the eGenes from the temporal cortex pyramidal neurons and the meta-analysis in our analysis of the fly screen hits.

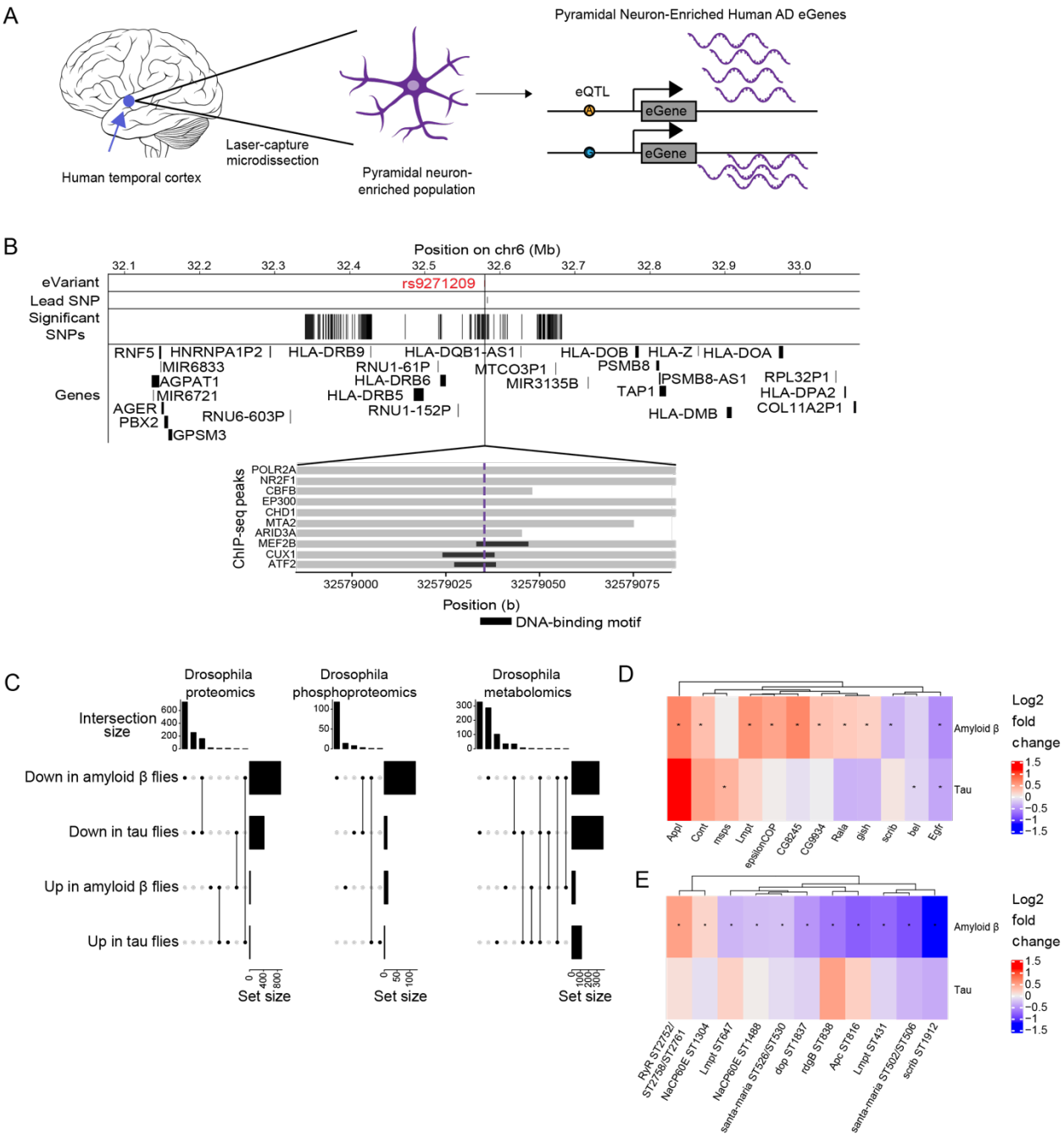

Figure 3. Multi-omic changes in human AD patients and model systems. A) Schematic depicting laser-capture microdissection of temporal cortex pyramidal neuron-enriched populations and identification of eGenes. Brain cartoon created with Biorender.com. B) The eQTL associated with the eGene HLA-DRB1 is highlighted in red and overlaps with DNA binding motifs of MEF2B, CUX1 and ATF2 derived from ENCODE ChIP-seq and FIMO-detected motifs. Grey horizontal bars indicate ChIP-seq binding regions and the black horizontal bars indicate where the DNA-binding motif is located. C) UpSet plots indicate the number of proteomic, phosphoproteomic, and metabolomic changes change in the same or different directions when comparing $A\beta_{1\text{-}42}$ transgenic flies (Amyloid β flies) to controls with those associated with comparing tau^{R406W} transgenic flies (tau flies) to controls. The top bar plot indicates how many changes fit into the

set depicted by the dots below, while the rightmost bar plot indicates the total number of proteins, phosphoproteins or metabolites that are upregulated in tau^{R406W} transgenic flies, downregulated in tau^{R406W} transgenic flies, upregulated in Aβ_{1-42} transgenic flies, or downregulated in Aβ_{1-42} transgenic flies. D) Heat maps depict the log2 fold changes between Aβ_{1-42} transgenic flies or tau^{R406W} transgenic flies with controls for D) proteins or E) phosphoproteins that were hits in the age-associated neurodegeneration screen. An asterisk indicates whether the comparison was significant at an FDR threshold of 0.1. The columns of all heatmaps were clustered by hierarchical clustering.

Chromosome:base pair position (hg19)	Previously nominated GWAS candidate	eGene	eQTL	Ref/alt allele	*P*	Fixed effects regression coefficient
6:32626139	HLA-DRB1	C4A	rs6905975	C:G	1.53E-02	-0.319
8:27400592	CLU/PTK2B	EPHX2	rs66924402	A:C	4.63E-02	0.170
6:32627485	HLA-DRB1	HLA-DQA1	rs9273432	T:C	3.69E-02	-0.414
6:32608251	HLA-DRB1	HLA-DQA2	rs28383408	C:G	9.15E-03	0.428
6:32628030	HLA-DRB1	HLA-DQB1	rs9273471	G:A	2.49E-03	-0.866
6:32608820	HLA-DRB1	HLA-DQB1-AS1	rs9272670	C:T	3.35E-02	-0.390
6:32663564	HLA-DRB1	HLA-DQB2	rs5000634	A:G	3.95E-05	0.690
6:32579035	HLA-DRB1	HLA-DRB1	rs9271209	G:A	6.94E-07	-0.686
6:32574990	HLA-DRB1	HLA-DRB5	rs9271025	T:C	5.80E-04	-0.791
16:31154146	KAT8	PRSS36	rs1549299	G:A	3.04E-02	-0.393
7:100190116	ZCWPW1	PVRIG	rs2734895	T:C	2.99E-02	-0.446
6:47413226	CD2AP	RP11-385F7.1	rs6934735	A:T	4.43E-02	-0.333

Table 2. eQTLs linked to AD GWAS loci: eGenes and variants from an eQTL analysis of 75 human temporal cortex pyramidal neuron-enriched population. P-value from meta-analysis across 1087 human AD patients across 7 previously published studies is also reported. Beta coefficient indicates the association between gene expression of the eGene and presence of Alzheimer's disease. Chromosomal coordinates are reported according to the human genome reference hg19 and the hypothetical gene is the variant reported in Jansen et al. 2019 for that particular locus[11].

We hypothesized that some temporal cortex pyramidal neuron eQTLs influence eGene expression by disrupting transcription factor binding. We used the ENCODE 3 transcription factor ChIP-seq data to see which eQTLs overlapped transcription factor peaks and DNA-binding motifs (Figure 3B). We found that the eQTL (*rs9271209*) for *HLA-DRB1* overlapped with ChIP-seq peaks and DNA-binding motifs for the transcription factors MEF2B, CUX1 and ATF2 (Figure 3B). Patients with the *rs9271209* eQTL have reduced expression of *HLA-DRB1*, suggesting that this Alzheimer's disease-associated effect on gene expression could be mediated through inhibition of transcription factor binding (Figure 3B, Table 2).

Proteomics, phosphoproteomics and metabolomics from Drosophila models of tauopathy or amyloid β neurotoxicity suggest how neurodegeneration screen hits contribute to disease

We generated proteomic, phosphoproteomic and metabolomic data from the heads of established *Drosophila* models of amyloid β and tau toxicity to find relationships between the neurodegeneration screen hits and Alzheimer's disease toxic proteins[43,59] (Figure 1, Tables S4, S5, S6). Specifically, we modeled amyloid β pathology using a transgenic fly line expressing the human amyloid β_{1-42} isoform (Aβ_{1-42} transgenic flies)[59]. We modeled tau pathology using a well-

characterized transgenic fly line expressing human *MAPT* with the neurodegenerative disease-associated R406W point mutation (tau^{R406W} transgenic flies)[43]. We used tau^{R406W} transgenic flies because these flies display a modest, but detectable degree of neurodegeneration at 10 days of age[43]. We aged control and experimental flies for 10 days and measured proteomics, phosphoproteomics and metabolomics.

We were interested in the molecular changes associated with the different pathological toxic proteins of Alzheimer's disease and related disorders. The largest sets of differential proteins, phosphoproteins or metabolites were those that were downregulated in tau^{R406W} transgenic flies or Aβ_{1-42} transgenic flies only (Figure 3C, Benjamini-Hochberg FDR-adjusted p-value<0.1). Proteins downregulated in both Aβ_{1-42} transgenic flies and tau^{R406W} transgenic flies were enriched for enzymes that metabolize carboxylic acids, amino acids, and lipids (Figure S4, Benjamini-Hochberg FDR-adjusted p-value<0.1). Unbiased metabolomics confirmed some of the signals we saw in the enriched proteomic pathways (Figure S4, Benjamini-Hochberg FDR-adjusted p-value<0.1). A C32:1 diacylglyceride (DAG), a C34:1 DAG, and a modified amino acid 3-methylhistidine were significantly upregulated in Aβ_{1-42} transgenic flies and tau^{R406W} transgenic flies while a C43:0 triacylglyceride and a nicotinamide adenine dinucleotide were downregulated in both models (Figure S4). Additionally, we found that proteins that were upregulated in Aβ_{1-42} transgenic flies and tau^{R406W} transgenic flies were enriched for muscle development and cell adhesion (Figure S4).

We tested whether the neurodegeneration screen hits were differentially abundant in the proteomic and phosphoproteomic data to identify genes that were likely to be associated with Aβ- or tau-related pathways (Figures 3D and 3E, Benjamini-Hochberg FDR-adjusted p-value<0.1). The screen hits that were differentially abundant in the Aβ_{1-42} transgenic fly proteomics were enriched for biological processes pertaining to development and cognition (Figure S4H, Benjamini-Hochberg FDR-adjusted p-value<0.1). None of the screen hits were differentially phosphorylated in the tau^{R406W} transgenic flies, while there were 11 phosphopeptides found in neurodegeneration screen hits that were differentially phosphorylated in Aβ_{1-42} transgenic flies (Figure 3E). Among these, the *Drosophila* proteins Appl, gish and Egfr are part of the Gene Ontology term for cognition; Appl and gish were significantly upregulated, while Egfr was significantly downregulated (Figure 3D, Benjamini-Hochberg FDR-adjusted p-value<0.1). Egfr was also significantly downregulated in the tau^{R406W} transgenic fly proteomics (Figure 3D, Benjamini-Hochberg FDR-adjusted p-value<0.1). Since *Egfr* knockdown is associated with age-associated neurodegeneration in our forward genetic screen, our observation suggests that *Egfr* and its human ortholog *ERBB3* play a role in neuronal death and decline in the context of Alzheimer's disease pathology.

Network integration of AD Omics and novel genetic screening data identifies subnetworks representing biological processes underlying neurodegeneration

We performed network integration of our *Drosophila* neurodegeneration screen hits with Alzheimer's disease multi-omics to determine how the neurodegeneration screen hits contribute to human Alzheimer's disease (Figure 1). We integrated the hits from the

neurodegeneration screen with our human eGenes and *Drosophila* proteomics, phosphoproteomics and metabolomics, a previously published genome-scale screen for tau mediated neurotoxicity tau^{R406W} flies, previously published human AD proteomics, and previously published human lipidomics using the Prize-collecting Steiner Forest algorithm (PCSF) to build a protein-protein/protein-metabolite interaction network model of Alzheimer's disease[24,34,33] (Figures 1, and 4A, Table S7). The detailed results of this network are visualized in an interactive website (Methods, Data and Code availability). Louvain clustering of the network revealed subnetworks enriched for biological processes associated with Alzheimer's disease in previous studies, such as insulin signaling, postsynaptic activity, and double-stranded break repair[50–52,57,58,60–62] (Figure 4A). Subnetworks were also enriched for cell signaling pathways such as NOTCH signaling and hedgehog signaling that have not been previously characterized as hallmarks of neurodegeneration[58] (Figure 4A).

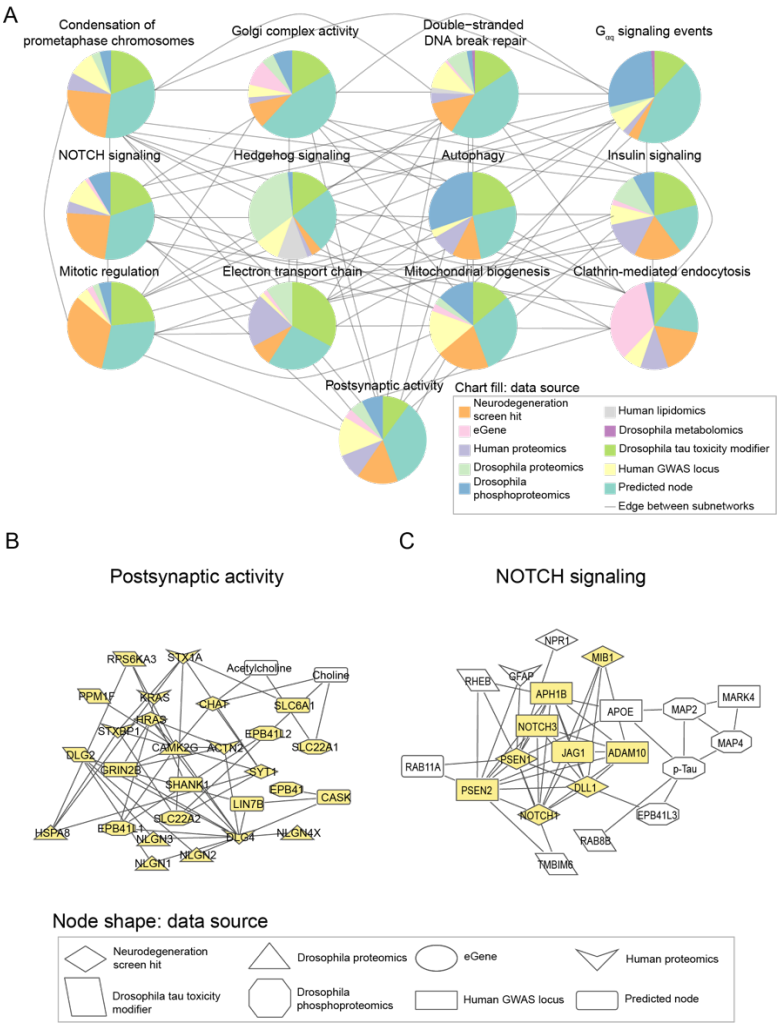

Figure 4. Network integration of Alzheimer's disease multi-omics and novel genetic screening data identifies subnetworks characterized by hallmarks of neurodegeneration and processes previously not implicated in Alzheimer's disease. A) Network integration of human and *Drosophila* multi-omics for Alzheimer's Disease highlights subnetworks enriched for proteins belonging to known gene ontologies. Each subnetwork is represented by a pie chart, which

indicates the proportion of nodes represented by a given data type. Edges indicate if at least one node in one subnetwork interacts with a node in the other subnetwork. Each pie chart is labeled by the enriched biological process by hypergeometric test (FDR-adjusted p-value less than 0.1). B) A subnetwork enriched for postsynaptic activity. Nodes belonging to the annotated process are highlighted in yellow. Also in this subnetwork are metabolites associated with postsynaptic activity such as acetylcholine. C) Phosphorylated tau, APOE, and APP-processing proteins interact with each other and are in a subnetwork enriched for NOTCH signaling-associated genes. Members of the NOTCH signaling pathway are highlighted in yellow.

We inspected the nodes of our network communities to determine whether the subnetworks represented expected or new relationships in the context of Alzheimer's disease. The subnetwork enriched for postsynaptic activity showed expected protein-metabolite and protein-protein interactions in choline metabolism[63,64] (Figure 4B). We observed interactions involving the metabolite acetylcholine with choline O-acetyl transferase (CHAT) and choline transporter (SLC22A1) (Figure 4B). Additionally, we saw interactions between choline, CHAT and choline transporters SLC22A1 and SLC22A2 (Figure 4B). This subnetwork illustrates the ability of our network analysis to recover established biological processes in Alzheimer's disease.

A novel role of NOTCH signaling emerged in one subnetwork that linking members of the pathway with phosphorylated tau, members of the gamma secretase complex, the APOE protein (Figure 4C). Each of these proteins has been associated with hallmarks of Alzheimer's disease[65–69]. However, the link between NOTCH signaling and amyloid β processing, neurofibrillary tangle formation or APOE variants has not previously been reported. These results suggest roles for NOTCH signaling proteins in Alzheimer's disease-mediated pathology.

Network integration of Alzheimer's disease Omics and genetic hits reveals targets that regulate tau-mediated neurotoxicity

We decided to experimentally test implications of a subnetwork linking a screen hit (*HNRNPA2B1)* and an eGene (*MEPCE*) with *Drosophila* modifiers of tau toxicity[24] (Figure 5A). We knocked down the fly orthologs of *HNRNPA2B1* or *MEPCE* in a *Drosophila* model of tauopathy with two independent RNAi lines per gene (Figure 5B, 5C). To enhance relevance to Alzheimer's disease in which wild type human tau is deposited, we used transgenic flies expressing wild-type human tau (tau^{WT}) in the fly retina[43]. We found that knockdown of fly orthologs of either *HNRNPA2B1* or *MEPCE* enhanced tau retinal toxicity, as quantified using a previously described semi-quantitative rating scale[70] (Figure 5B, 5C, one-way ANOVA with Tukey's post-hoc correction $p<0.05$). The fly data are consistent with the human eQTL results, which show that *MEPCE* expression is reduced in Alzheimer's disease patients with the eQTL *rs7798226* (Table S3) and suggest a mechanism for effects of the GWAS variant in Alzheimer's disease.

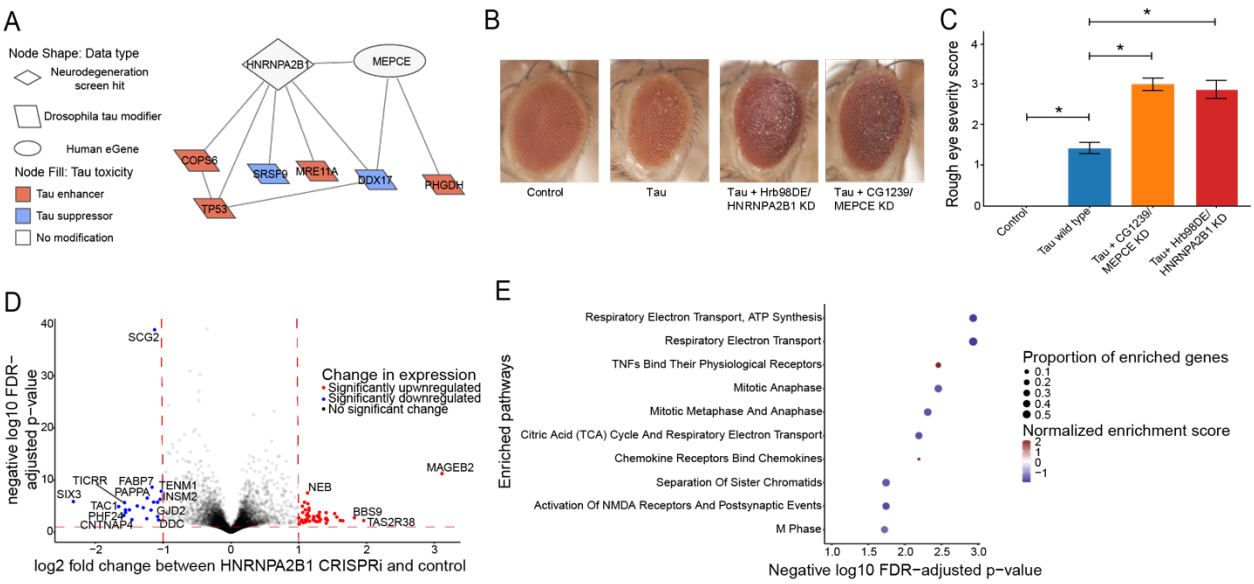

Figure 5. Network integration of AD mulit-omics and novel genetic screening data reveals biological processes associated with tau-mediated neurotoxicity. A) The neurodegeneration modifier *HNRNPA2B1* and the eGene *MEPCE* interact with each other and have protein-protein interactions with modifiers of tau neurotoxicity. The interaction between HNRNPA2B1 and MEPCE is found in the subnetwork in figure 4 that is enriched for insulin signaling. B) Knock-down of the *Drosophila* orthologs of *HNRNPA2B1* (*Hrb98DE*) and *MEPCE* (*CG1293*) shows enhancement of the rough eye phenotype in flies expressing wild type human tau. Control is *GMR-GAL4/+*. n=8. Flies are one day old. Two independent RNAi constructs were used to knock down each gene. C) Quantification of rough eye severity. Statistical significance was measured using a one-way ANOVA with Tukey's post-hoc correction and is indicated with an asterisk. Error bars are the standard error of the mean. D) Volcano plot depicting differential expression analysis by DeSeq2 of bulk RNA-seq after *HNRNPA2B1* CRISPRi knockdown in NGN2 neural progenitor cells (Benjamini-Hochberg FDR<0.1, absolute $\log_2$ fold change > 1). Each dot represents a single gene. The horizontal dashed line indicates the negative $\log_{10}$ FDR-adjusted p-value significance cut-off of 0.1 and the vertical dashed lines indicate the $\log_2$ fold change cut-offs of 1 and -1. Red dots indicate genes that are significantly upregulated and blue dots indicate genes that are significantly downregulated. E) Dot plot of the enriched pathways identified by gene set enrichment analysis of the RNA-seq data. The 10 pathways with the highest negative $\log_{10}$ FDR-adjusted p-value are plotted. The size of the dot indicates the proportion of genes that are part of the enriched pathway. The color of the dot represents the normalized enrichment score (NES), where blue indicates downregulation and red indicates upregulation. The x-position of the dot indicates the negative $\log_{10}$ FDR-adjusted p-value and the y-position is the corresponding, enriched pathway.

To understand how *HNRNPA2B1* contributes to age-associated neurodegeneration in human systems, we performed RNA-seq after CRISPRi knockdown of *HNRNPA2B1* in human iPSC-derived, NGN2 neural progenitor cells. Our knockdown achieved a partial reduction of *HNRNPA2B1* gene relative to control (Figure S5A, $\log_2$(Fold Change)=-0.60, Benjamini-Hochberg

FDR-adjusted p-value<0.1). Differential expression after *HNRNPA2B1* knockdown showed that the most significantly downregulated genes involved those involved in neuronal development or synaptic activity such as *SCG2*, *FABP7*, *TENM1*, and *SIX3* (Figure 5D; Table S8, $\log_2$(Fold Change)<-1, Benjamini-Hochberg FDR-adjusted p-value<0.1). Gene Set Enrichment Analysis showed that the top enriched pathways include downregulation of the electron transport chain and of genes involved in postsynaptic events (Figure 5E; Table S9, Benjamini-Hochberg FDR-adjusted p-value<0.1). Reduced postsynaptic activity and electron transport chain activity have been previously associated with Alzheimer's disease and tau-mediated neurotoxicity[57,71–76]. These changes suggest potential roles for how *HNRNPA2B1* contributes to tau-mediated neurotoxicity and neurodegeneration in human aging.

Network analysis implicates neurodegeneration genes as regulators of the Alzheimer's disease-associated biological process of DNA damage repair

In addition to the network connections between NOTCH signaling proteins and hallmark proteins of Alzheimer's disease (Figure 4C), we also noted many links between NOTCH signaling proteins were associated with the Alzheimer's disease-associated process of DNA damage, a process also associated with Alzheimer's disease[60–62,77–79](Figure 6A). Some of these interacting partners were shared with another neurodegeneration screen hit, *CSNK2A1* (Figure 6A). All the interacting DNA damage repair-associated nodes that interact with *CSNK2A1* and *NOTCH1* except for *H2AFX* and *COPS2* regulate double-stranded break repair, suggesting that *CSNK2A1* and *NOTCH1* knockdown may disrupt this process.

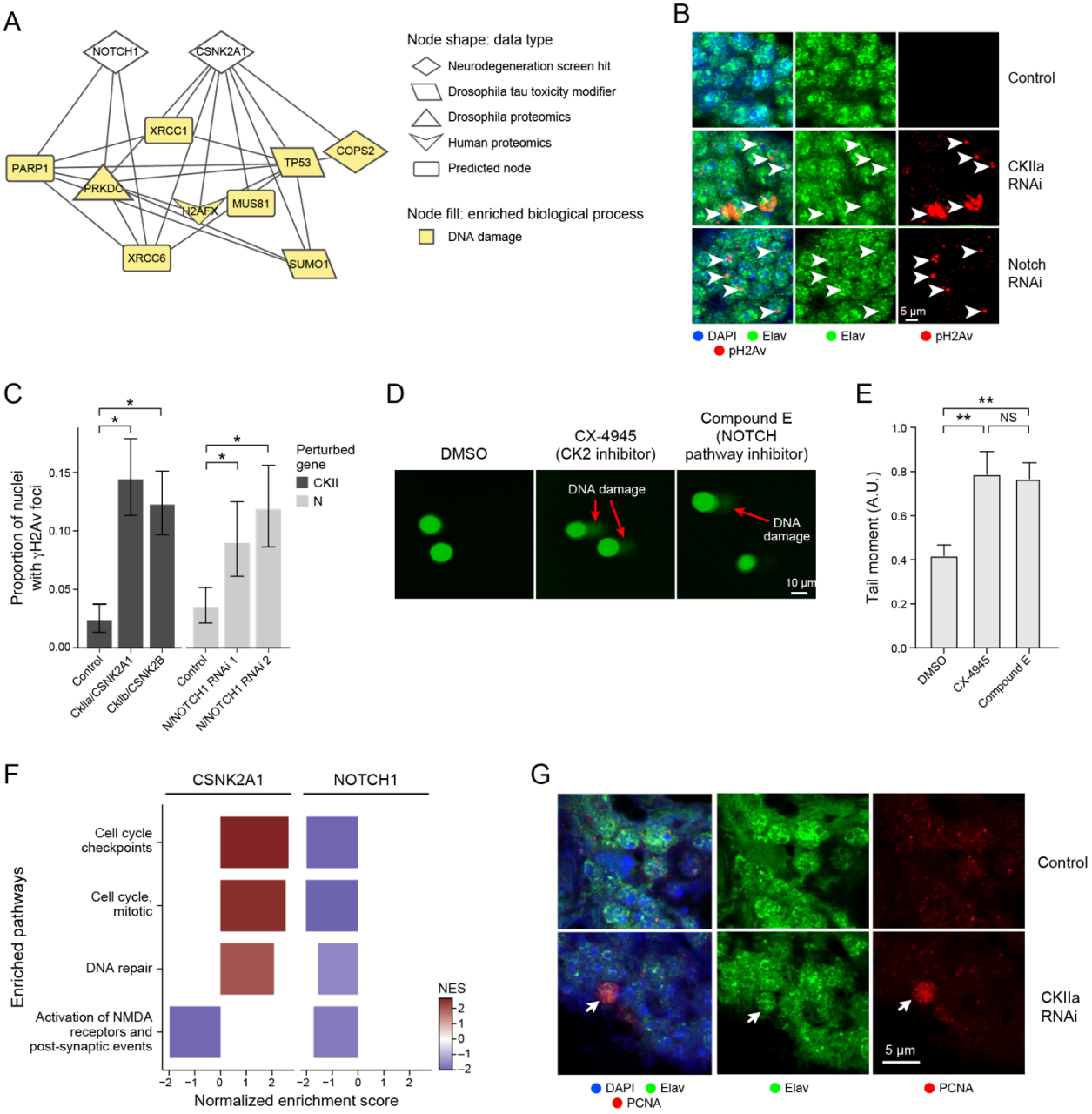

Figure 6. Network analysis implicates neurodegeneration genes as regulators of the AD-associated biological process of DNA damage repair. A) NOTCH1 and CSNK2A1 interact with AD-specific omics that are involved in DNA damage repair processes. Nodes involved in DNA damage are highlighted in yellow. B) Immunofluorescence shows that knockdown of *Drosophila* orthologs for *NOTCH1* and *CSNK2A1* lead to increased DNA damage in the fly. DNA damage is assayed by immunostaining for phosphorylated H2Av (pH2Ax, red). Brain cortex neurons are identified by elav immunostaining (green). Nuclei are identified with DAPI immunostaining (blue). n=6. Flies are 10 days old. Controls are *elav-GAL4/+; UAS-Dcr-2/+* (CkIIa and CkIIb knockdowns) or *elav-GAL4/+* (N knockdown). The scale bar represents 5 µm. C) Percent of nuclei containing γH2AX foci in control flies, *Drosophila* knockdowns of orthologs of CSNK2A1 (CKIIa and CKIIb) and NOTCH1 (N). Asterisks indicate significance of a one-way binomial test

after Benjamini-Hochberg FDR correction p<0.01. Error bars are 95% binomial confidence intervals. n=6. Flies are 10 days old. Controls are *elav-GAL4/+; UAS-Dcr-2/+* (CKII knockdown) or *elav-GAL4/+* (N knockdown). D) Inhibition of Casein Kinase 2 (CK2) by CX-4945, and the inhibition of NOTCH cleavage by Compound E enhances DNA damage in human iPSC-derived neural progenitor cells measured by the COMET assay. E) Quantification of the tail moments from panel A in arbitrary units. Asterisks indicate p<0.01 by ANOVA with Tukey's Post-Hoc correction. Error bars indicate standard error of the mean. F) Bar plots showing the normalized enrichment scores (NES) of selected, significantly enriched REACTOME pathways after CSNK2A1 and NOTCH1 knockdown in NGN2 neural progenitor cells. Red and blue bars indicate positive and negative NES, respectively, reflecting upregulation or downregulation of pathways. Pathways were selected to show shared changes in pathways related to cell cycle, DNA repair and postsynaptic activity. G) Representative immunofluorescence images show inappropriate cell cycle re-entry in postmitotic neurons as indicated by PCNA expression (red, arrow) following CK2 knockdown. The neuronal marker elav identifies neurons (arrows). PCNA, the neuronal promoter elav and DAPI are represented in red, green, and blue respectively.

Next, we used RNAi to knock down *Drosophila* orthologs of *NOTCH1* and *CSNK2A1* in a pan-neuronal pattern in aging adult flies to assess the relationship between these neurodegeneration screen hits and DNA damage (Figures 6B and 6C). We used two RNAi molecules targeting the *NOTCH1* ortholog N (Figures 6B and 6C). For *CSNK2A1* we used one RNAi to target the *CkIIa* subunit of the casein kinase holoenzyme and another RNAi to target the *CkIIb* subunit of the casein kinase holoenzyme because many of the available CkII RNAi lines were lethal when used for pan-neuronal knockdown (Figures 6B and 6C). We observed that knockdown of the *Drosophila* orthologs for *NOTCH1* and *CSNK2A1* led to an increase in DNA damage, as measured by γH2AX foci (Figures 6B and 6C, One-Way Binomial Test p<0.01).

We performed a COMET assay in wild-type human neuronal progenitor cells treated with inhibitors for the Notch signaling pathway or the casein kinase holoenzyme (CK2) to test if reduced *CSNK2A1* or *NOTCH1* function leads to increased DNA damage in human cells (Figures 6D and 6E). We observed that treatment with the Notch inhibitor Compound E and the CK2 inhibitor CX-4945 led to an increase in the tail moment of the neural progenitor cells compared to DMSO treatment, showing an increase in DNA damage after inhibitor treatment (Figure 6D and 6E, ANOVA with Tukey's post-hoc correction p-value<0.01, Methods). These results show how the screen hits *NOTCH1* and *CSNK2A1* regulate DNA damage in human and *Drosophila* neurons, as inferred by our computational network analysis.

Transcriptomic analysis suggests how CSNK2A1 and NOTCH1 knockdown could lead to age-associated neurodegeneration through distinct DNA-damaging pathways

We performed RNA-seq after CRISPRi knockdown of *CSNK2A1* or *NOTCH1* in NGN2-expressing neural progenitor cells to broadly understand how human cells respond to reduced *CSNK2A1* and *NOTCH1* expression (Figure 6). Expression of both target genes dropped significantly in the

respective knockdowns (*CSNK2A1*: $\log_2$(fold change)<-1, FDR-adjusted p-value<0.1, Figure S5B; *NOTCH1:* $\log_2$(fold change)=-0.92, FDR-adjusted p-value<0.1, Figure S5C), with good clustering of replicates in PCA analysis (Figure S5D). We found 145 significantly upregulated and 282 significantly downregulated genes upon knocking down *CSNK2A1*, while we found 15 significantly upregulated and 5 significantly downregulated genes after knocking down *NOTCH1* (Figure S6A and S6B; Table S8, absolute value of $\log_2$(fold change)>1, FDR-adjusted p-value<0.1). The disparity in the number of differentially expressed genes could be explained by how the knockdown efficiency of *NOTCH1* was less than that of *CSNK2A1* (Figure S5A and S5B).

Gene Set Enrichment Analysis of RNA-seq data after CRISPRi knockdown of *CSNK2A1* and *NOTCH1* in NGN2 neural progenitor cells suggested that both genes regulated DNA damage repair pathways. However, we were surprised to find that these pathways were regulated in different directions for each knockdown (Figure 6F; Table S7). This analysis showed that cell cycle and DNA damage repair pathways were upregulated upon *CSNK2A1* knockdown while these same pathways were downregulated upon *NOTCH1* knockdown (Figure 6F). To determine if *CSNK2A1* knockdown led to inappropriate activation of cell cycle regulators in postmitotic neurons, we knocked down a *Drosophila* ortholog of *CSNK2A1* (*CkIIa*) and assessed changes in proliferating cell nuclear antigen (PCNA), a robust marker of cell cycle activation in *Drosophila* and mammalian systems[80–82] (Figures 6F and 6G). We found an increase in PCNA following *CKIIa* knockdown by immunofluorescence, supporting our hypothesis that knockdown of *CKIIa* promotes neuronal activation of cell cycle regulators (Figure 6G). As expected, there was no PCNA activation in control post-mitotic neurons (Figure 6G). Activation of cell cycle proteins in mature neurons is associated with Alzheimer's disease, cell death, and double strand break-bearing neurons[80,83–86]. These results suggest that *CSNK2A1* knockdown could lead to neurodegeneration through neuronal cell cycle re-entry and the accumulation of DNA damage-bearing neurons.

Discussion

Starting from an unbiased genetic screen for modifiers of aging-related neurodegeneration, we computationally and experimentally identified several of the pathways downstream of the screen hits. One highlight of our work is the demonstration that *CSNK2A1* and *NOTCH1* regulate age-associated neurodegeneration through DNA damage response pathways (Figures 5, 6). Our work suggests a new direction in understanding DNA damage in aging and disease and finding ways to modulate it. Previous studies showed that that HDAC inhibitors reduced DNA damage burden and neuronal cell death[60,77–79,87–89]. Other studies have proposed neuroprotective compounds that inhibit cell cycle re-entry in post-mitotic neurons like we observed upon *CSNK2A1* knockdown[90].

Future work could explore cause-and-effect relationships between DNA damage and activation of cell cycle genes in the context of *CSNK2A1* knockdown. Currently, the causal relationship between cell cycle regulators and DNA damage in neurodegeneration is unclear[91]. One hypothesis supported by our results is that *CSNK2A1* knockdown leads to neurodegeneration by activating genes that promote DNA replication and entry into the G_1 phase of the cell cycle,

amplifying existing DNA damage in the neuron (Figures 6D and 6E). Alternatively, our work also suggests that excess accumulation of DNA damage upon *CSNK2A1* knockdown could lead to inappropriate activation of cell cycle regulators and DNA repair proteins to fix DNA damage (Figures 6D and 6E). Understanding the causes or consequences of DNA damage can help inform neuroprotective approaches for limiting age-associated DNA damage.

In another advance from this study, we suggest how change in *MEPCE* expression contributes to neuronal death in Alzheimer's disease (Figure 5). Our eQTL analysis showed that patients that inherited the *rs7798226* eQTL had reduced *MEPCE* expression and our experimental data shows that reduced expression of *MEPCE* enhances tau toxicity in the fly (Table S2, Figures 5B, 5C). Future studies could investigate whether the downregulation of *MEPCE* in patients with the *rs7798226* eQTL is strong enough to induce tau-mediated neurotoxicity in humans. This example illustrates how multi-omic network integration identified pathways potentially downstream of a disease-causing variant. Our network analysis work identified an eQTL that may play a role in Alzheimer's disease-mediated neurodegeneration, which is an inference that could not be made from fine-mapping analysis alone.

We acknowledge that some of our network findings differ from expectations in the literature. We found from our network analysis and subsequent experimentation in human tau transgenic flies that knockdown of *HNRNPA2B1* led to increased age-associated neurodegeneration and increased tau-mediated neurotoxicity (Figure 5). However, *HNRNPA2B1* was upregulated in Alzheimer's disease excitatory neurons in the largest published single nucleus RNA-seq study in human Alzheimer's disease[79]. Another study showed that *HNRNPA2B1* knockdown in iPSC-derived neurons and mouse hippocampal neurons was protective against oligomeric tau-mediated neurotoxicity[92]. In the context of these studies, our results suggest that the *HNRNPA2B1* is under tight control; significant changes in *HNRNPA2B1* homeostasis may have consequences on tauopathy. Additionally, the effect of *HNRNPA2B1* on tau-mediated neurotoxicity relative to the overexpression of tau^{WT} could be different than that associated with the presence of oligomeric tau. The effect of *HNRNPA2B1* knockdown could also be different in the fly retina from its effect in the mouse hippocampus.

Our work illustrates an analytical framework that can be applied to other neurodegenerative diseases. The genetic screen for age-associated neurodegeneration was intentionally broad, with genes knocked out in a pan-neuronal pattern to maximize recovery of neurodegeneration hits. We observed that a significant proportion of age-associated genes in multiple human brain tissues are enriched for neurodegeneration screen hits (Figure 2D). Given the diversity of brain regions affected in aging-related disorders, some of the screen hits are likely associated with diseases other than AD, and some may influence more than one disease. Pathways that influence multiple diseases would be particularly important for therapeutic strategies to prevent aging of the brain. Previous work has used protein-protein interactions as a lens for looking at genes that underlie protein aggregation in multiple neurodegenerative diseases[93]. The framework presented in this paper could be used to combine the screen hits with appropriate disease-specific data to search for disease-universal or disease-specific regulators across neurodegenerative diseases. We also note that while our genetic screen data was

neuron-specific, future work could use network analysis approaches presented in this or other studies to screens in other non-neuronal cell types[13,94].

Methods

Data and Code availability

RNA-seq data from neural progenitor cells and temporal cortex pyramidal neurons will be deposited into the Gene Expression Omnibus (GEO) by the time of manuscript publication. The full network in Figure 4 is available and explorable at https://fraenkel-lab.github.io/neurodegeneration-network/.

Code can be found at https://github.com/fraenkel-lab/neurodegeneration-network and is publicly available as of the date of publication.

Additional data needed to reanalyze the data reported in this paper is available from the lead contact upon request.

Drosophila *stocks and Genetics*

All fly crosses and aging were performed at 25°C. Equal numbers of adult male and female flies were analyzed. For the genome-scale screen, brain histology was examined at 30 days post-eclosion. Flies were aged to 10 days post-eclosion for brain proteomics, metabolomics, and histology. The *UAS-tau wild type, UAS-tau^{R406W} and UAS-Aβ$^{1-42}$* transgenic flies been described previously[43,59]. Expression of human tau or amyloid β was directed to neurons using the pan-neuronal driver *elav-GAL4* or to the retina using the *GMR-GAL4* driver. Dcr-2 was expressed in some animals to enhance RNAi-mediated gene knockdown. Transgenic RNAi lines for genome-scale gene knockdown were obtained from the Bloomington *Drosophila* Stock Center and from the Vienna *Drosophila* Resource Center. The following stocks were also obtained from the Bloomington *Drosophila* Stock Center: *elav-GAL4, GMR-GAL4, UAS-CG1239 (MEPCE) RNAi HMC02896, UAS-CG1239 (MEPCE) RNAi HMC04088, UAS-Hrb98DE (HNRNPA2B1) RNAi HMC00342, UAS-Hrb98DE (HNRNPA2B1) RNAi JF01249, UAS-CkIIα RNAi JF01436, UAS-CkIIβ RNAi JF01195, UAS-N RNAi 1 (GLV21004), UAS-N RNAi 2 (GL0092), UAS-Dcr-2*.

Histology, immunostaining, and imaging

For examination of the adult fly brain, animals were fixed in formalin and embedded in paraffin. 4 μm serial frontal sections were prepared through the entire brain and placed on a single glass slide. Hematoxylin and eosin staining was performed on paraffin sections to assess brain integrity. For immunostaining of paraffin sections, slides were processed through xylene, ethanol, and into water. Antigen retrieval by boiling in sodium citrate, pH 6.0, was performed prior to blocking. Blocking was performed in PBS containing 0.3% Triton X-100 and 2% milk for 1 hour and followed by incubation with appropriate primary antibodies overnight. Primary antibodies to the following proteins were used at the indicated concentrations: pH2Av (Rockland,

600-401-914, 1:100), elav (Developmental Studies Hybridoma Bank, 9F8A9 at 1:20 and 7E8A10 at 1:5) and PCNA (DAKO, MO879, 1:500). For immunofluorescence studies, Alexa 555- and Alexa 488-conjugated secondary antibodies (Invitrogen) were used at 1:200. For quantification of pH2Av, a region of interest comprised of approximately 100 Kenyon neurons was identified in well-oriented sections of the mushroom body and the number of neurons containing one or more than one immuno-positive foci was determined. Images were taken on Zeiss LSM800 confocal microscope (Carl Zeiss, AG), and quantification was performed using Image-J software. For all histological analyses, at least 6 brains were analyzed per genotype and time point. The sample size (n), mean and SEM are given in the figure legends. Representative images were obtained using a Zeiss LSM 800 confocal microscope. All acquisition parameters were kept the same for all experimental groups.

Quantitative Mass Spectrometry sample preparation for proteomics

Three control (genotype: *elav-GAL4/+),* three tau (genotype: *elav-GAL4/+; UAS-tau^{R406W}/+),* and three $A\beta_{1-42}$ (genotype: *elav-GAL4/+; UAS-Aβ$^{1-42}$)* samples of approximately 350 fly heads each were used for proteomic analysis. Samples were prepared as previously described[95] with the following modifications. All solutions are reported as final concentrations. *Drosophila* heads were lysed by sonication and passaged through a 21-gauge needle in 8 M urea, 200 mM EPPS, pH 8.0, with protease and phosphatase inhibitors (Roche). Protein concentration was determined with a micro-BCA assay (Pierce). Proteins were reduced with 5 mM TCEP at room temperature for 15 minutes and alkylated with 15 mM Iodoacetamide at room temperature for one hour in the dark. The alkylation reaction was quenched with dithiothreitol. Proteins were precipitated using the methanol/chloroform method. In brief, four volumes of methanol, one volume of chloroform, and three volumes of water were added to the lysate, which was then vortexed and centrifuged to separate the chloroform phase from the aqueous phase. The precipitated protein was washed with one volume of ice-cold methanol. The protein pellet was allowed to air dry. Precipitated protein was resuspended in 200 mM EPPS, pH 8. Proteins were digested with LysC (1:50; enzyme:protein) overnight at 25^{o}C followed by trypsin (1:100; enzyme:protein) for 6 hours at 37 ^{o}C. Peptide quantification was performed using the micro-BCA assay (Pierce). Equal amounts of peptide from each sample was labeled with tandem mass tag (TMT10) reagents (1:4; peptide:TMT label) (Pierce). The 10-plex labeling reactions were performed for 2 hours at 25^{o}C. Modification of tyrosine residues with TMT was reversed by the addition of 5% hydroxyl amine for 15 minutes at 25^{o}C. The reaction was quenched with 0.5% trifluoroacetic acid and samples were combined at a 1:1:1:1:1:1:1:1:1:1 ratio. Combined samples were desalted and offline fractionated into 24 fractions as previously described.

Liquid chromatography-MS3 spectrometry (LC-MS/MS)

12 of the 24 peptide fractions from the basic reverse phase step (every other fraction) were analyzed with an LC-MS3 data collection strategy on an Orbitrap Lumos mass spectrometer (Thermo Fisher Scientific) equipped with a Proxeon Easy nLC 1000 for online sample handling and peptide separations[96]. Approximately 5 µg of peptide resuspended in 5% formic acid + 5% acetonitrile was loaded onto a 100 µm inner diameter fused-silica micro capillary with a needle

tip pulled to an internal diameter less than 5 µm. The column was packed in-house to a length of 35 cm with a C_{18} reverse phase resin (GP118 resin 1.8 µm, 120 Å, Sepax Technologies). The peptides were separated using a 180 min linear gradient from 3% to 25% buffer B (100% acetonitrile + 0.125% formic acid) equilibrated with buffer A (3% acetonitrile + 0.125% formic acid) at a flow rate of 600 nL/min across the column. The scan sequence began with an MS1 spectrum (Orbitrap analysis, resolution 120,000, 350−1350 *m/z* scan range, AGC target 1×10^6, maximum injection time 100 ms, dynamic exclusion of 75 seconds). The "Top10" precursors were selected for MS2 analysis, which consisted of CID (quadrupole isolation set at 0.5 Da and ion trap analysis, AGC 1.5×10^4, NCE 35, maximum injection time 150 ms). The top ten precursors from each MS2 scan were selected for MS3 analysis (synchronous precursor selection), in which precursors were fragmented by HCD prior to Orbitrap analysis (NCE 55, max AGC 1.5×10^5, maximum injection time 150 ms, isolation window 2 Da, resolution 50,000).

LC-MS3 data analysis

A suite of in-house software tools was used for .RAW file processing and controlling peptide and protein level false discovery rates, assembling proteins from peptides, and protein quantification from peptides as previously described[96]. MS/MS spectra were searched against a Uniprot *Drosophila* reference database appended with common protein contaminants and reverse sequences. Database search criteria were as follows: tryptic with two missed cleavages, a precursor mass tolerance of 50 ppm, fragment ion mass tolerance of 1.0 Da, static alkylation of cysteine (57.02146 Da), static TMT labeling of lysine residues and N-termini of peptides (229.162932 Da), and variable oxidation of methionine (15.99491 Da). TMT reporter ion intensities were measured using a 0.003 Da window around the theoretical *m/z* for each reporter ion in the MS3 scan. Peptide spectral matches with poor quality MS3 spectra were excluded from quantitation (<200 summed signal-to-noise across 10 channels and <0.7 precursor isolation specificity).

Metabolomics

Three control (genotype: *elav-GAL4/+),* three tau (genotype: *elav-GAL4/+; UAS-tau^{R406W}/+),* and three $A\beta_{1\text{-}42}$ (genotype: *elav-GAL4/+; UAS-Abeta$^{1\text{-}42}$)* samples of 40 fly heads each were collected and untargeted positively and negative charged polar and non-polar metabolites were assessed using liquid chromatography-mass spectrometry as described in detail previously[97].

Identifying Age-Associated Genes in RNA-seq data from the Genotype-Tissue Expression (GTEx) project

To identify what genes had significant associations between gene expression in the brain and chronological age, we sought out RNA-seq data sets with many individuals and a large dynamic range of ages. We analyzed 2642 samples from 382 individuals representing 13 different brain tissues, using the measurements of transcripts per million (TPM) available from the GTEx analysis version 8 (https://gtexportal.org/home/datasets). The age range of the patients are from 20-70 years old with a median age of 58 years old. To measure the effects of age on gene

expression in the brain, we used a mixed-effects model as implemented in lme4 version 1.1.27.1, treating sex, ethnicity, patient identity and tissue of origin as covariates with the following equation:

Y ~ Age + Sex + PMI + Tissue + Ethnicity + Sample ID

Where "Sample ID" is treated as a random effect while all other covariates are treated as fixed effects. We identify genes as significantly associated with age if the FDR-adjusted p-value for the age coefficient is less than 0.1 and if the absolute unstandardized coefficient for age is greater than 0.1, which corresponds to a change of 1 TPM per decade in this data set, assuming age is the only factor. We used this equation to assess whether there was a significant effect on gene expression with age given the mean expression of the screen hits. To assess robustness of this test, we performed 10,000 permutations of either gene sets of the same size as the set of the screen hits or over patient age. We computed an empirical p-value which was the number of permutations with p-values smaller than the original test divided by the number of permutations. When performing this analysis for individual tissues, we used a generalized additive model with the same formula but excluding the "Sample ID" and "Tissue" variables.

To perform Gene Set Enrichment Analysis, we used the R package "fgsea" version 1.14.0 using the Reactome 2022 library from Enrichr as the reference set of pathways. We used the standardized regression coefficient to rank the genes[47,98].

Analysis of single-nuclear RNA-seq data

To identify cellular subtypes that were associated with disease, we analyzed previously published single nuclear RNA-seq data[46], which included 70,000 cells from 24 Alzheimer's disease patients and 24 age and sex-matched healthy controls. The data were preprocessed as in previous work[46]. In short, for each of the previously defined "broad cell types" (excitatory neurons, inhibitory neurons, astrocytes, oligodendrocytes, microglia and oligodendrocyte progenitor cells), we applied Seurat version 4.0.4's implementations for log-normalizing the data, detecting highly variable features, and standard scaling the data. We used Seurat's implementation of PCA reducing the data to 20 principal components. After applying PCA, we used Harmony version 0.1 to correct for the effects of sex, individual, sequencing batch and post-mortem interval in our data. This correction was performed to minimize the effects of confounders in our clustering analysis. We further applied Scrublet to predict and remove doublet cells from the population as implemented in Scanpy version 1.8.2. We used the Harmony components for UMAP dimensionality reduction and Leiden clustering. To determine the Leiden clustering resolution, we calculated the silhouette coefficient after applying Leiden clustering on a range of values (resolution={0.1,0.2,0.3,0.4, 0.6, 0.8, 1.0, 1.4, 1.6, 2.0,2.1,2.2,2.3,2.4,2.5}). We selected the clustering resolution that maximized the silhouette coefficient. To identify disease-associated clusters, we applied a hypergeometric test to determine if a cluster was over-represented by cells derived from Alzheimer's disease patients or healthy controls. We subsequently applied MAST as implemented in Seurat to determine the differentially expressed genes between Alzheimer's disease-enriched clusters and the

remaining sub-clusters within a given cell type. We defined differentially expressed genes as having an FDR-adjusted p-value less than 0.1 and an absolute $\log_2$ fold change greater than 1.

Analysis of Drosophila *multi-omics*

We performed two-way t-tests to assess the significance of *Drosophila* proteins, phosphoproteins and metabolites between *Drosophila* models of amyloid β and control as well as significant proteins, phosphoproteins and metabolites between *Drosophila* models of tau and control. We used gProfiler with the g_SCS multiple hypothesis correction to identify significant gene ontology terms using *Drosophila* pathways as a reference[99]. We used PiuMet to map unannotated m/z peaks in the metabolomic data to known compounds[100].

Fluorescence microscopy

Confocal images were taken on a Zeiss LSM-800 confocal microscope with Airyscan.

Laser-capture RNA-seq

We used the laser-capture RNA-seq method to profile total RNA of brain neurons similar to what we reported in previous studies[31,32]. In brief, laser-capture microdissection was performed on human autopsy brain samples to extract neurons[32]. For each temporal cortex (middle gyrus) about 300 pyramidal neurons were outlined in layers V/VI by their characteristic size, shape, and location in HistoGene-stained frozen sections and laser-captured using the Arcturus Veritas Microdissection System (Applied Biosystems) as in previous studies[32]. Linear amplification, construction, quantification, and quality control of sequencing libraries, fragmentation, and sequencing methods were described in earlier studies[32]. RNA seq data processing and quality control was performed similar to what we reported in previous studies[31,32]. In summary, The RNA-sequencing data was aligned to the human genome reference sequence hg19 using TopHat v2.0 and Cufflinks v1.3.0. To measure RNA-sequencing quality control, we used FASTQC and RNA-SeQC. We blinded ourselves to the disease status of the patient when preparing the samples.

Data sets used for expression Quantitative Trait Locus (eQTL) analysis

eQTL analysis was performed using seven previously published bulk cortex data sets and one new laser-captured pyramidal neuron data set. ROSMAP, MayoRNAseq, MSBB, and HBTRC data were obtained from the AD Knowledge Portal (https://adknowledgeportal.org) on the Synapse platform (Synapse ID: syn9702085). CommonMind was obtained from the CommonMind Consortium Knowledge Portal (https://doi.org/10.7303/syn2759792) also on the Synapse platform (Synapse ID: syn2759792); GTEx was obtained from https://gtexportal.org/home/. UKBEC, was obtained from http://www.braineac.org/; BRAINCODE, was obtained from http://www.humanbraincode.org/. The data sets are described in detail at each of the source portals and in the corresponding original publications[31,32,101–109].

We used a conservative four-stage design: ***1***, Cortex discovery stage: eQTL analysis in four human cortex cohorts (stage D in Supplementary Table 1**)**. ***2***, Cortex replication stage: replication of findings from the discovery stage in three independent human cortex cohorts (stage R in Supplementary Table 1). ***3***, To further enhance statistical power, we performed meta-analysis across all seven cohorts. This meta-analysis highlighted an additional 17 suggestive eGenes with *P* values $\leq 5 * 10^{-8}$ (Table S2) which were not recovered in the two-stage design. 4, We confirmed 12 suggestive eGenes in the laser-captured pyramidal neuron data set with P values ≤ 0.05.

Gene expression data processing

For RNAseq data sets, the gene reads counts were normalized to TPM (Transcripts Per Kilobase Million) by scaling gene length first and followed by scaling sequencing depth. The gene length was considered as the union of exon lengths. Consistent and stringent quality control and normalization steps were applied for each of the cohorts: 1) For sample quality control, we removed samples with poor alignment. We kept samples with > 10M mapped reads and > 70% mappability by considering reads with mapping quality of Q20 or higher (the estimated read alignment error rate was 0.01 or less). 2) Filtering sample mix-ups by comparing the reported sex with the transcriptional sex determined by the expression of female-specific *XIST* gene and male-specific *RPS4Y1* gene. 3) Filtering sample outliers. Sample outliers with problematic gene expression profiles were detected based on Relative Log Expression (RLE) analysis, spearman correlation based hierarchical clustering, D-statistics analysis[110]. 4) For normalization, gene expression values were quantile normalized after log10 transformed by adding a pseudo count of 1e-4. 5) SVA package was applied for removing batch effects by using combat function and adjusting age, sex, RIN, PMI. We accounted for latent covariates by performing fsva function. Residuals were outputted for downstream analysis. For array-based gene expression datasets, we directly used the downloaded, quality-controlled gene expression profiles.

Genotype data processing for eQTL analyses

We applied PLINK2 (v1.9beta) and in house scripts to perform rigorous subject and SNP quality control (QC) for each dataset in the following order: 1) Set heterozygous haploid genotypes as missing; 2) remove subjects with call rate < 95%; 3) remove subjects with gender misidentification; 4) remove SNPs with genotype call rate < 95%; 5) remove SNPs with Hardy-Weinberg Equilibrium testing P value $< 1 \times 10^{-6}$; 6) remove SNPs with informative missingness test (Test-mishap) P value $< 1 \times 10^{-9}$; 7) remove SNPs with minor allele frequency (MAF) < 0.05; 8) remove subjects with outlying heterozygosity rate based on heterozygosity F score (beyond 4*sd from the mean F score); 9) IBS/IBD filtering: pairwise identity-by-state probabilities were computed for removing both individuals in each pair with IBD>0.98 and one subject of each pair with IBD > 0.1875; (10) population substructure was tested by performing principal component analysis (PCA) using smartPCA in EIGENSOFT[111]. PCA outliers were excluded and the top 3 principal components were used as covariates for adjusting population substructures.

Imputation of Genotypes for eQTL analyses

The array-based genotype datasets were enhanced by genotype imputation. Genotype imputation for each dataset was performed separately on Michigan Imputation Server, using

1000G phase 3 reference panel. Eagle v2.3 and Minimac3 were selected for phasing and imputing respectively, and EUR population was selected for QC. Only variants with R^2 estimates less than or equal to 0.3 were excluded from further analysis. And only variants with MAF > 5% were also included in downstream eQTL analysis. Prior to imputation, pre-imputation checks provided by Will Rayner performed external quality controls to fit the requirements of the imputation server. We used European population reference (EUR) haplotype data from the 1000 Genomes Project (2010 interim release based on sequence data freeze from 4 August 2010 and phased haplotypes from December 2010) to impute genotypes for up to 6,709,258 SNPs per data set. We excluded SNPs that did not pass quality control in each study

eQTL analysis

The eQTL mapping was conducted using R Package Matrix EQTL using the additive linear model on a high-performance Linux-based Orchestra cluster at Harvard Medical School. For cis-eQTL analysis, SNPs were included if their positions were within 1Mb with the TSS of a gene. And trans-eQTL analysis included SNP-gene association if their distance was beyond this window. FDRs reported by MatrixEQTL were used to estimate the association between SNPs and gene expression.

Meta eQTL analysis

We performed meta eQTL analysis using three separate effects model implemented in METASOFT[112], which took effect size and standard error of SNP-gene pair in each dataset as input. Fixed effects model (FE model) was based on inverse-variance-weighted effect sizes. Random Effects model (RE model) was a very conservative model based on inverse-variance-weighted effect size. Han and Eskin's random effects model (RE2 model) was optimized to detect associations under heterogeneity. We reported statistics of the RE2 model in this study.

Identifying eGene-associated variants that associate with transcription factor binding

We were interested in determining whether eGene-associated variants overlapped with transcription factor binding sites. We used the optimal hg19 ChIP-seq-derived transcription factor peak sets from ENCODE 3, which we downloaded from the UCSC genome browser. To determine if the eQTL of interest overlapped with a DNA-binding motif, we extracted the sequence 50 base pairs upstream and 50 base pairs downstream of the variant and used FIMO to detect the presence of an overlapping DNA-binding motif[113]. We used the HOCOMOCO version 11 core motif set as reference motifs. Correlations between *HLA-DRB1* and *CUX1* expression were performed using Pearson's correlation test as implemented in R version 4.0.2.

To identify correlations between eGenes and biological pathways, we applied GSVA version 1.42.0 to the CPM-normalized temporal cortex pyramidal neuron RNA-seq to identify the REACTOME pathway enrichments per-sample. For this analysis we used the REACTOME pathways available in GSVAdata version 1.30, which downloads the REACTOME pathways from msigdb version 3.0 with the data set named "c2BroadSets". We calculated correlations between GSVA signatures and gene expression using the Pearson correlation coefficient as

implemented in R version 4.0.2, considering correlations with an FDR-adjusted p-value less than 0.1.

Design of integration analyses

In order to identify the biological mechanisms through which human and model organism genetic hits contribute to neurodegenerative disease, we utilized the Prize-Collecting Steiner Forest algorithm (PCSF) as implemented in OmicsIntegrator 2[36] (OI v2.3.10, https://github.com/fraenkel-lab/OmicsIntegrator2). The PCSF algorithm identifies disease-associated networks based on termini derived from sequencing data that is significantly altered in individuals with the disease. We used OmicsIntegrator to map proteomic, phosphoproteomic, metabolomic and genetic changes to a set of known protein-protein and protein-metabolite interactions derived from physical protein-protein interactions from iRefIndex version 17 and protein-metabolite interactions described in the HMDB and Recon 2 databases. To add brain-specific edges, we include the interactions derived from Affinity Purification Mass Spectrometry (AP-MS) of mice in BraInMap[114]. Additionally, we include previously published interactions between proteins found in tau aggregates and phosphorylated tau derived from AP-MS of neurofibrillary tangles[115]. The costs on the protein-protein interactions were computed as 1 minus the edge score reported by iRefIndex, while the cost of the protein-metabolite interactions were calculated as in previous studies[100,116]. Given that these reference interactions were defined in human proteins and metabolites, we mapped the *Drosophila* proteins and phosphoproteins to their human orthologs using DIOPT version 8.0, choosing the human orthologs that the tool determined were of "moderate" or "high" confidence[117] (https://www.flyrnai.org/cgi-bin/DRSC_orthologs.pl). In order to comprehensively characterize metabolomic changes, we used PiuMet to map uncharacterized metabolites to compounds identified in HMDB[100]. In addition to integrating the phosphoproteomic data, we included the predicted upstream kinases from iProteinDB whose proteomic levels in *Drosophila* correlated with its phosphoproteomic targets[118] (Spearman correlation coefficient>0.4, https://www.flyrnai.org/tools/iproteindb/web/).

For the Alzheimer's disease-specific network, we integrated the screen hits with genetic modifiers of disease severity from model organism screens and available proteomics, phosphoproteomics and metabolomics from the literature and generated data. Given the breadth and diversity of sequencing data for Alzheimer's disease, we applied different thresholds of significance for each source of sequencing data to generate the Alzheimer's disease network. The prizes of the proteomic, phosphoproteomic, and metabolomic data are calculated as the negative base 10 logarithm of the Benjamini-Hochberg FDR-corrected p-value calculated by a two-way t-test. The *Drosophila* phosphoproteomic data and the metabolomic data were subject to an FDR threshold of 0.1, while the *Drosophila* proteomic and human proteomic data had more stringent cutoffs (FDR<0.01 and FDR<0.0001 respectively). Additionally, the metabolomic data were only assigned prizes if the absolute $\log_2$ fold change was greater than 1. The human lipidomic data were assigned prizes by their negative $\log_{10}$ nominal p-value and were included if their nominal p-value was less than 0.05. The upstream kinases were assigned the same prizes as the targeted phosphoproteins. Instead of assigning

prizes based on a two-way t-test, the genetic hits were assigned prizes differently. For the human eGenes, prizes were assigned to all genes in the discovery phase with a value equal to -$\log_{10}$(genome-wide FDR). For genes found in the *Drosophila* neurodegeneration and tau aggregation screens, prizes were set to 1=-$\log_{10}$(0.1). For the human GWAS loci, the prizes were set to the -$\log_{10}$ Bonferroni corrected, genome-wide p-value for those determined to be causal loci according to previous analyses and 1 otherwise[12]. After the initial prize assignments, the values are minimum-maximum normalized to values between 0 and 1 within each data type, weighing each prize by a scale factor reflecting our confidence in the degree to which a given data type reflects Alzheimer's disease pathology (Table S7). We further included previously published *Drosophila* modifiers of tau toxicity[24].

For each network, we performed 100 randomizations of the edges with gaussian noise to assess the robustness of the nodes to perturbations to edges and prize values. Additionally, we performed 100 randomizations of the prize values to assess the specificity of each node to their assigned prizes. We filtered out nodes that did not have a prize (Steiner nodes) if they appeared in fewer than 40 of the robustness randomizations and more than 40 of the specificity randomizations. We then performed Louvain and Greedy clustering for community detection in the networks.

OmicsIntegrator hyperparameters control the weights on prizes (β), the weight of the edges on the dummy node for network size (ω) and the edge penalty for highly connected "hub" nodes (γ). In order to select hyperparameters for OmicsIntegrator, we evaluated a range of hyperparameters for each network: β={2,5,10}, ω={1,3,6} and γ={2,5,6}. We chose networks based on minimizing the mean specificity, maximizing the mean robustness, and minimizing the KS statistic between node degree of the prizes as compared to those of the predicted nodes.

Networks were visualized using Cytoscape version 3.8.0.

COMET assay for DNA damage in human neural progenitor cells

For the alkaline COMET assay, we applied inhibitors of CK2 (CX-4945) and the NOTCH signaling pathway (Compound E) to human iPSC-derived neural progenitor cells. Cells were treated with 5µM of the inhibitor overnight and harvested. Comets were selected using the OpenComet plugin in ImageJ[88,119]. The extent of DNA damage was measured by the tail moment and proportion of intensity between the tail and the head of the comet. The tail represents single-stranded DNA that trails off from the nucleus due to DNA damage burden. Longer tails indicate a greater extent of DNA damage. DMSO and etoposide were included as negative and positive controls respectively.

Human iPSC culture

Human iPSCs (male WTC11 background, gift from the lab of Michael Ward) harboring a single-copy of doxycycline-inducible (DOX) mouse NGN2 at the AAVS1 locus and pC13N-dCas9-BFP-KRAB at human CLYBL intragenic safe harbor locus (between exons 2 and 3) were cultured in

mTeSR Medium (Stemcell Technologies; Cat. No. 85850) on Corning Tissue Culture Treated Dishes (VWR International LLC; Cat. No. 62406-161) coated with Geltrex (Life Technologies Corporation; Cat. No. A1413301). Briefly, mTESR medium supplemented with mTESR supplement (Stemcell Technologies; Cat. No. 85850) and antibiotic Normocin (Invivogen; Cat. No. Ant-nr-2) was replenished every day until 50% confluent[26]. Stem cells were transduced with lentivirus packaged with CROPseq-Guide-Puro vectors and selected with Puromycin (Gibco; Cat. No. A11138-03) until confluent. When cells were 80%-90% confluent, cells were passaged, which entailed the following: dissociating in Accutase (Stemcell Technologies; Cat. No. 7920) at 37°C for 5 minutes, diluting Accutase 1:5 with mTeSR medium, collecting in conicals and centrifuging at 300g for 5 minutes, asipirating supernatant, resuspending in mTESR supplemented with 10uM Y-27632 dihydrochloride ROCK inhibitor (Stemcell Technologies; Cat. No. 72302) and plating in Geltrex-coated plates.

NGN2 Neuronal Differentiation and RNA extraction

Neuronal differentiation was performed as described in previous work with a few modifications[120]. On day 1, iPSCs transduced with CROPseq-Guide-Puro were plated at 40,000 cells/cm^2 density in Geltrex-coated tissue culture plates in mTESR medium supplemented with ROCK inhibitor and 2µg/ml Doxycycline hyclate (Sigma; Cat. No. D9891-25G). On Day 2, Medium was replaced with Neuronal Induction media containing the following: DMEM/F12 (Gibco; Cat. No 11320-033), N2 supplement (Life Technologies Corporation; Cat. No. 17502048), 20% Dextrose (VWR; Cat. No. BDH9230-500G), Glutamax (Life Technologies Corporation; Cat. No. 35050079), Normocin (Invivogen; Cat. No. Ant-nr-2), 100 nM LDN-193189 (Stemcell Technologies; Cat. No. 72147), 10uM SB431542 (Stemcell Technologies; Cat. No. 72234) and 2uM XAV (Stemcell Technologies; Cat. No. 72674) and 2µg/ml DOX. The Neuronal Induction Media was replenished on day 3. On day 4, the medium was replaced with Neurobasal Media (Life Technologies Corporation; Cat. No. 21103049) containing B27 supplement (Gibco; Cat. No. 17504044), MEM Non-Essential Amino Acids (Life Technologies Corporation; Cat. No. 11140076) Glutamax, 20% Dextrose, 2µg/ml DOX, Normocin, 10ng/ml BDNF (R&D Systems; Cat. No. 11166-BD), 10ng/ml CNTF (R&D Systems; Cat. No. 257-NT/CF), 10ng/ml GDNF (R&D Systems; Cat. No. 212-GD/CF) and cultured for 2 days. At day 6, cells were dissociated with Accutase and resuspended with Trizol (Thermofisher Scientific; Cat. No.15596018). RNA was extracted following manufacturer's manual, using Direct-zol RNA Miniprep kit (Zymo Research, R2050)

Bulk RNA-seq analysis of CRISPRi knockdowns in neural progenitor cells

We analyzed the RNA-seq data after CRISPRi knockdown as performed in previous CRISPRi studies[27]. In summary, we mapped the raw sequencing reads to the hg38 reference transcriptome with salmon version 1.10.1. We used the '-noLengthCorrection' option to generate transcript abundance counts. We generated gene-level count estimates with tximport version 1.16.1. To account for the effects of different guides, we performed differential expression analysis between knockdown and control with DESeq2 version 1.28.1 treating guide identity as a covariate. We applied the apelgm package version 1.10.0 to shrink the $\log_2$ fold

changes. We applied Gene Set Enrichment Analysis to the ranked, shrunk log_2 fold changes using the fgsea package version 1.14.0 and the Reactome 2022 library as the reference pathway set[47,98].

Acknowledgements

We thank Leslie Gaffney for assistance with figure design and thank all members of the Fraenkel lab for their feedback on the project and manuscript. We thank the MIT BioMicroCenter for RNA sequencing of the NGN2 neural progenitor cells. M.J.L. was supported in part by the Barbara Weedon Fellowship. Fly stocks were obtained from the Bloomington Drosophila Stock Center (NIH P40-OD018537) and the Vienna Drosophila Resource Center. We thank the Transgenic RNAi Project (TRiP) at Harvard Medical School (NIH R24 OD030002; PI: N. Perrimon) for making Drosophila stocks[121]. Monoclonal antibodies were obtained from the Developmental Studies Hybridoma Bank developed under the auspices of the NICHD and maintained by the University of Iowa, Department of Biology, Iowa City, IA 52242. Yi Zhong provided excellent technical assistance. This research was funded by NIH R01-AG057331 to E.F., C.R.S., and M.B.F. The results published here are in whole or in part based on data obtained from the AD Knowledge Portal (https://adknowledgeportal.org). The ROSMAP study data were provided by the Rush Alzheimer's Disease Center, Rush University Medical Center, Chicago. Data collection was supported through funding by NIA grants P30AG10161 (ROS), R01AG15819 (ROSMAP; genomics and RNAseq), R01AG17917 (MAP), R01AG36836 (RNAseq), U01AG32984 (genomic and whole exome sequencing), U01AG61356 (whole genome sequencing, targeted proteomics, ROSMAP AMP-AD), the Illinois Department of Public Health (ROSMAP), and the Translational Genomics Research Institute (genomic). The MSBB data were generated from postmortem brain tissue collected through the Mount Sinai VA Medical Center Brain Bank and were provided by Dr. Eric Schadt from Mount Sinai School of Medicine. The Mayo RNAseq study data was led by Dr. Nilüfer Ertekin-Taner, Mayo Clinic, Jacksonville, FL as part of the multi-PI U01 AG046139 (MPIs Golde, Ertekin-Taner, Younkin, Price). Samples were provided from the following sources: The Mayo Clinic Brain Bank. Data collection was supported through funding by NIA grants P50 AG016574, R01 AG032990, U01 AG046139, R01 AG018023, U01 AG006576, U01 AG006786, R01 AG025711, R01 AG017216, R01 AG003949, NINDS grant R01 NS080820, CurePSP Foundation, and support from Mayo Foundation. Study data includes samples collected through the Sun Health Research Institute Brain and Body Donation Program of Sun City, Arizona. The Brain and Body Donation Program is supported by the National Institute of Neurological Disorders and Stroke (U24 NS072026 National Brain and Tissue Resource for Parkinsons Disease and Related Disorders), the National Institute on Aging (P30 AG19610 Arizona Alzheimers Disease Core Center), the Arizona Department of Health Services (contract 211002, Arizona Alzheimers Research Center), the Arizona Biomedical Research Commission (contracts 4001, 0011, 05-901 and 1001 to the Arizona Parkinson's Disease Consortium) and the Michael J. Fox Foundation for Parkinsons Research. For the CommonMind study, Data were generated as part of the CommonMind Consortium supported by funding from Takeda Pharmaceuticals Company Limited, F. Hoffman-La Roche Ltd and NIH grants R01MH085542, R01MH093725, P50MH066392, P50MH080405, R01MH097276, RO1-MH-075916, P50M096891, P50MH084053S1, R37MH057881, AG02219, AG05138, MH06692, R01MH110921, R01MH109677, R01MH109897, U01MH103392, U01MH116442, project ZIC

MH002903 and contract HHSN271201300031C through IRP NIMH. Brain tissue for the study was obtained from the following brain bank collections: The Mount Sinai/JJ Peters VA Medical Center NIH Brain and Tissue Repository, the University of Pennsylvania Alzheimer's Disease Core Center, the University of Pittsburgh Brain Tissue Donation Program, and the NIMH Human Brain Collection Core. CMC Leadership: Panos Roussos, Joseph Buxbaum, Andrew Chess, Schahram Akbarian, Vahram Haroutunian (Icahn School of Medicine at Mount Sinai), Bernie Devlin, David Lewis (University of Pittsburgh), Raquel Gur (University of Pennsylvania), Chang-Gyu Hahn (Thomas Jefferson University), Enrico Domenici (University of Trento), Mette A. Peters, Solveig Sieberts (Sage Bionetworks), Stefano Marenco, Barbara K. Lipska, Francis J. McMahon (NIMH).

Author contributions

M.J.L., C.R.S., M.B.F., and E.F. conceived of and designed the study. C.A.Z, H.B., and M.B.F, designed and performed all experiments in *Drosophila*. M.J.L. performed computational analysis of published human bulk and single-cell RNA-seq, differential *Drosophila* proteomics, phosphoproteomics and metabolomics, multi-omic network integration, and RNA-seq analysis of iPSC-derived neural progenitor cells. J.P.,T.W.,D.G.,Z.L., X.D., and C.R.S. designed and performed laser-capture microdissection and eQTL meta-analysis. P-C.P. and L-H.T. designed and performed COMET assay in iPSC-derived neural progenitor cells. B.K., S.D., J.B., R.N., and S.F. designed and performed iPSC-derived motor neuron differentiation and RNA-seq experiments. M.J.L., M.B.F., and E.F. wrote the manuscript. C.R.S., M.B.F., and E.F. provided funding for the study.

References

1. Martin, J.B. (1999). Molecular Basis of the Neurodegenerative Disorders. N. Engl. J. Med *340*, 1970–1980.

2. Wilson, R.S., Segawa, E., Boyle, P.A., Anagnos, S.E., Hizel, L.P., and Bennett, D.A. (2012). The natural history of cognitive decline in Alzheimer's disease. Psychol. Aging *27*, 1008–1017.

3. Goedert, M., and Spillantini, M.G. (2006). A Century of Alzheimer's Disease. Science *314*, 777–780.

4. Lee, V.M.-Y., Goedert, M., and Trojanowski, J.Q. (2001). Neurodegenerative Tauopathies. Annu. Rev. Neurosci *24*, 1121–1159.

5. De Strooper B and Karran E (2016). The Cellular Phase of Alzheimer's Disease. Cell *164*, 603–615.

6. Selkoe, D.J., and Hardy, J. (2016). The amyloid hypothesis of Alzheimer's disease at 25 years. EMBO Mol Med *8*, 595–608. 10.15252/emmm.201606210.

7. Hutton, M., Lendon, C.L., Rizzu, P., Baker, M., Froelich, S., Houlden, H., Pickering-Brown, S., Chakraverty, S., Isaacs, A., Grover, A., et al. (1998). Association of missense and 5′-splice-site mutations in tau with the inherited dementia FTDP-17. Nature *393*, 702–705. 10.1038/31508.

8. Lunn, J.S., Sakowski, S.A., Hur, J., and Feldman, E.L. (2011). Stem Cell Technology for Neurodegenerative Diseases. Ann. Neurol *70*, 353–361.

9. Raj, T., Li, Y.I., Wong, G., Humphrey, J., Wang, M., Ramdhani, S., Wang, Y.-C., Ng, B., Gupta, I., Haroutunian, V., et al. (2018). Integrative transcriptome analyses of the aging brain implicate altered splicing in Alzheimer's disease susceptibility. Nat. Genet *50*, 1584–1592.

10. Kunkle, B.W., Grenier-Boley, B., Sims, R., Bis, J.C., Damotte, V., Naj, A.C., Boland, A., Vronskaya, M., Lee, S.J., Amlie-Wolf, A., et al. Alzheimer Disease Genetics Consortium, European Alzheimer's Disesase Initiative, Cohorts for Heart and Aging Research in Genome Epidemiology Consortium, and Genetic and Environmental Risk in AD/Defining Genetic Polygenic and Environmental Risk for Alzheimer's Disease Consortium (2019) Genetic meta-analysis of diagnosed Alzheimer's disease identifies new risk loci and implicates Aβ, tau, immunity and lipid processing. Nat. Genet *51*, 414–430.

11. Jansen, I.E., Savage, J.E., Watanabe, K., Bryois, J., Williams, D.M., Steinberg, S., Sealock, J., Karlsson, I.K., Hägg, S., Athanasiu, L., et al. (2019). Genome-wide meta-analysis identifies new loci and functional pathways influencing Alzheimer's disease risk. Nat. Genet *51*, 404–413.

12. Corces, M.R., Scherbina, A., Kundu, S., Gloudemans, M.J., Frésard, G., JM, L., BH, E., T, S., S, B., ST, M., et al. (2020). Single-cell epigenomic analyses implicate candidate causal variants at inherited risk loci for Alzheimer's and Parkinson's disease. Nat. Genet *52*, 1158–1168.

13. Roussaire, J.-P., Gao, V., Rodriguez-Rodriguez, P., Oughtred, R., Rust, J., Plautz, Z., Kasturia, S., Albornoz, C., Want, W., Schmidt, E.F., et al. (2020). Selective neuronal vulnerability in Alzheimer's disease: a network-based analysis. Neuron *107*, 821–835.

14. Bellenguez, C., Küçükali, F., Jansen, I.E., Kleineidam, L., Moreno-Grau, S., Amin, N., Nai, A.C., Campos-Marin, R., Grenier-Boley, B., and Andrade, V. (2022). New insignts into the genetic etiology of Alzheiemer's disease and related dementias. Nat. Genet *54*, 412–436.

15. Scherzer, C.R., Jensen, R.V., Gullans, S.R., and Feany, M.B. (2003). Gene expression changes presage neurodegeneration in a Drosophila model of Parkinson's disease. Human Molecular Genetics *12*, 2457–2466. 10.1093/hmg/ddg265.

16. Scherzer, C.R., Offe, K., Gearing, M., Rees, H.D., Fang, G., Heilman, C.J., Schaller, C., Bujo, H., Levey, A.I., and Lah, J.J. (2004). Loss of Apolipoprotein E Receptor LR11 in Alzheimer Disease. Archives of Neurology *61*, 1200–1205. 10.1001/archneur.61.8.1200.

17. Pearl R. and Parker S.L. (1921). Experimental studies on the duration of life. I. Introductory discussion of the duration of life in Drosophila. Am. Nat *55*, 481–509.

18. Piper, M.D.W. and Partridge L. (2018). Drosophila as a model for ageing. Biochim. Biophys. Acta. Mol. Basis Dis *1864*, 2707–2717.

19. St. Johnston D (2002). The art and design of genetic screens: Drosophila melanogaster. Nat. Rev. Genet *3*, 176–188.

20. Ugur, B., Chen, K., and Bellen, H.J. (2016). Drosophila tools and assays for the study of human diseases. Dis Model Mech *9*, 235–244. 10.1242/dmm.023762.

21. Grotewiel, M.S., Martin, I., Bhandari, P., and Cook-Wiens, E. (2005). Functional senescence in *Drosophila melanogaster*. Ageing Research Reviews *4*, 372–397. 10.1016/j.arr.2005.04.001.

22. Iliadi, K.G., Knight, D., and Boulianne, G.L. (2012). Healthy Aging – Insights from Drosophila. Frontiers in Physiology *3*.

23. Tamura, T., Chiang, A.-S., Ito, N., Liu, H.-P., Horiuchi, J., Tully, T., and Saitoe, M. (2003). Aging Specifically Impairs amnesiac-Dependent Memory in Drosophila. Neuron *40*, 1003–1011. 10.1016/S0896-6273(03)00732-3.

24. Lohr, K.M., Frost, B., Scherzer, C., and Feany, M.B. (2020). Biotin rescues mitochondrial dysfunction and neurotoxicity in a tauopathy model. Proc. Natl. Acad. Sci. U.S.A *117*, 33608–33618.

25. Wertz, M.H., Mitchem, M.R., Pineda, S.S., Hachigian, L.J., Lee, H., Lau, V., Powers, A., Kulicke, R., Madan, G.K., and M, C. (2020). Genome-wide in vivo CNS screening identifies genes that modify CNS neuronal survival and mHTT toxicity. Neuron *106*, 1–14.

26. Tian, R., Gachechiladze, M.A., Ludwig, C.H., Laurie, M.T., Hong, J.Y., Nathaniel, D., Prabhu, A.V., Fernandopulle, M.S., Patel, R., Abshari, M., et al. (2019). CRISPR Interference-Based Platform for Multimodal Genetic Screens in Human iPSC-Derived Neurons. Neuron *104*, 239–244.

27. Tian, R., Abarientos, A., Hong, J., Hashemi, S.H., Yan, R., Dräger, L., K, N., MA, S., AB, X., K, F., et al. (2021). Genome-wide CRISPRi/a screens in human neurons link lysosomal failure to ferroptosis. Nat. Neurosci *24*, 1020–1034.

28. Hof, P.R., Cox, K., and Morrison, J.H. (1990). Quantitative analysis of a vulnerable subset of pyramidal neurons in Alzheimer's disease: I. Superior frontal and inferior temporal cortex *301*, 44–54.

29. Arnold, S.E., Hyman, B.T., Flory, J., Damasio, A.R., and Hoesen, G.W. (1991). The Topological and Neuroanatomical Distribution of Neurofibrillary Tangles and Neuritic

Plaques in the Cerebral Cortex of Patients with Alzheimer's Disease. Cereb. Cortex *1*, 103–116.

30. Emert-Buck, M.R., Bonner, R.F., Smith, P.D., Chuaqui, R.F., Zhuang, Z., Goldstein, W., SR, RA, and Liotta, L.A. (1996). Laser capture microdissection. Science *274*, 998–1001.

31. Dong, X., Liao, Z., Gritsch, D., Hadzhiev, B., Y, L., JJ, G., B, L., G, B., Wang, T., Adler, C.H., et al. (2018). Enhancers active in dopamine neurons are a primary link between genetic variation and neuropsychiatric disease. Nat. Neurosci *21*, 1482–1492.

32. Dong, X., Bai, Y., Liao, Z., Gritsch, D., Liu, X., Wang, T., Borges-Monroy, R., Ehrlich, A., Serrano, G.E., Feany, M.B., et al. (2023). Circular RNAs in the human brain are tailored to neuron identity and neuropsychiatric disease. Nat Commun *14*, 5327. 10.1038/s41467-023-40348-0.

33. Blanchard, J.W., Akay, L.A., Davila-Velderrain, J., Maydell, D., Mathys, H., Davidson, S.M., Effenberger, A., Chen, C.-Y., Maner-Smith, K., Hajjar, I., et al. (2022). APOE4 impairs myelination via cholesterol dysregulation in oligodendrocytes. Nature *611*, 769–779.

34. Johnson, E.C.B., Dammer, E.B., Duong, D.M., Ping, L., Zhou, M., Yin, L., Higginbotham, L.A., Guajardo, A., White, B., Troncoso, J.C., et al. (2020). Large-scale proteomic analysis of Alzheimer's disease brain and cerebrospinal fluid reveals early chages in energy metabolism associated with microglia and astrocyte activation. Nat. Med *26*, 769–780.

35. Tuncbag, N., Braunstein, A., Pagnani, A., Huang, S.-S.C., Chayes, J., Borgs, C., Zecchina, R., and Fraenkel, E. (2013). Simultaneous Reconstruction of Multiple Signaling Pathways via the Prize-Collecting Steiner Forest Problem. J. Comp. Biol *20*, 124–136.

36. Tuncbag, N., Gosline, S.J.C., Kedaigle, A., Soltis, A.R., Gitter, A., and Fraenkel, E. (2016). Network-based interpretation of diverse high-throughput datasets through the Omics Integrator software package. PLoS Comput. Bio *12*, 1004879.

37. Wang, L., Xia, J., Li, J., Hagemann, T.L., Fraenkel, JR Jones, Weitz E, Zhang DA, Messing A. S-C, and Feany, M.B. (2018). Tissue and cellular rigidity and mechanosensitive signaling activation in Alexander disease. Nat. Commun *9*, 1–14.

38. Archer, T.C., Ehrenberger, T., Mundt, F., Gold, M.P., Krug, K., Mah, C.K., Mahoney, E.L., Daniel, C.J., LeNail, A., and D, R. (2018). Proteomics, Post-translational Modifications, and Integrative Analyses Reveal Molecular Heterogeneity within Medulloblastoma Subgroups. Cancer Cell *34*, 396–410.

39. Sarkar, S., Murphy, M.A., Dammer, E.B., Olsen, A.L., Rangaraju, S., Fraenkel, E., and Feany, M.B. (2020). Comparative proteomic analysis highlights metabolic dysfunction in α-synucleinopathy. NPJ Parkinsons Dis *6*, 1–14.

40. NeuroLINCS Consortium, Li, J., Lim, R.G., Kaye, J.A., Dardov, V., Coyne, A.N., Wu, J., Milani, P., Cheng, A., Thompson, T.G., et al. (2021). An integrated multi-omic analysis of iPSC-derived motor neurons from C9ORF72 ALS patients. iScience *24*, 103221. 10.1016/j.isci.2021.103221.

41. Nithianandam, V., Bukhari, H., Leventhal, M.J., Battaglia, R.A., Dong, X., Fraenkel, E., and Feany, M.B. (2023). Integrative analysis reveals a conserved role for the amyloid precursor protein in proteostasis during aging. Nat. Commun *14*, 1–19.

42. Buchanan, R.L., and Benzer, S. (1993). Defective glia in the Drosophila brain degeneration mutant drop.

43. Wittmann, C.W., Wszolek, M.F., Shulman, J.M., Salvaterra, P.M., Lewis, J., Hutton, M., and Feany, M.B. (2001). Tauopathy in Drosophila: neurodegeneration without neurofibrillary tangles. Science *293*, 711–714.

44. Ordonez, D.G., Lee, M.K., and Feany, M.B. (2018). α-synuclein Induces Mitochondrial Dysfunction through Spectrin and the Actin Cytoskeleton. Neuron *98*, 108-124.e6.

45. Heisenberg, M., and Böhl, K. (XXXX). Isolation of Anatomical Brain Mutants of Drosophila by Histological. Z Naturforsch, 143–147.

46. Mathys, H., Davila-Velderrain J, Peng Z, Gao F, Mohammadi S, Young JZ, Menon M, He L, Abdurrob F, Jiang X, et al. (2019). Single- Cell Transcriptomic Analysis of Alzheimer's disease. Nature *570*, 332–337.

47. Croft, D., O'Kelly, G., Wu, G., Haw, R., Gillespie, M., Matthews, L., Caudy, M., Garapati, P., Gopinath, G., Jassal, B., et al. (2011). Reactome: a database of reactions, pathways and biological processes. Nucleic Acids Res *39*, 691–697.

48. Iqbal, K., Zidi, T., Wen, G.Y., Grundke-Iqbal, I., Merz, P.A., Shaikh, S.S., Wisniewski, H.M., Alafuzoff, I., and Winblad, B. (1986). Defective brain microtubule assembly in Alzheimer's disease. The Lancet *328*, 421–426.

49. Selkoe, D.J. (2003). Folding proteins in fatal ways. Nature *426*, 900–904.

50. Watson GS and Craft S (2004). Moculation of memory by insulin and glucose: neuropsychological observations in Alzheimer's disease. Eur. J. Pharmacol *490*, 97–113.

51. Bedse, G., Domenico, F., Serviddio, G., and Cassano, T. (2015). Aberrant insulin signaling in Alzheimer's disease: current knowledge. Front. Neurosci *9*, 204.

52. Stanley, M., Macauley, S.L., and Holtzman, D.M. (2016). Changes in insulin and insulin signaling in Alzheimer's disease: cause or consequence? J. Exp. Med *213*, 1375–1385.

53. Grubman, A., Chew, G., Ouyang, J.F., Sun, G., Choo, X.Y., Mclean, C., Simmons, R.K., Buckberry, S., Vargas-Landin, D.B., Poppe, D., et al. (2019). A single-cell atlas of entorhinal cortex from individuals with Alzheimer's disease reveals cell-type-specific gene expression regulation. Nat. Neurosci *22*, 2087–2097.

54. Zhou, Y., Song, W.M., Andhey, P.S., Swain, A., Levy, T., Miller, K.R., Poliani, P.L., Cominelli, M., Grover, S., Gilfillan, S., et al. (2020). Human and mouse single-nucleus transcriptomics reveal TREM2-dependent and TREM2- independent cellular responses in Alzheimer's disease. Nat. Med *26*, 131–142.

55. Lau, S.-F., Cao, H., Fu, A.K.Y., and Ip, N.Y. (2020). Single-nucleus transcriptome analysis reveals dysregulation of angiogenic endothelial cells and neuroprotective glia in Alzheimer's disease. Proc. Natl. Acad. Sci. U.S.A *117*, 25800–25809.

56. Davila-Velderrain, J., Mohammadi S, Ruzicka B, Jiang X, Ng A, Bennett DA, Tsai L-H, and Kellis M (2021). Single-cell anatomical analysis of human hippocampus and entorhinal cortex uncovers early-stage molecular pathology in Alzheimer's disease. Preprint at BioRxiv. https://doi.org/10.1101/2021.07.01.450715.

57. Murdock, M., and Tsai, L.-H. (2023). Insights into Alzheimer's disease from single-cell genomic approaches. Nat. Neurosci *26*, 181–195.

58. Wilson III, DM, MR, C., L, D.B., H, Z., DM, H., and I, D. (2023). Hallmarks of neurodegenerative diseases. Cell *186*, 693–706.

59. Finelli, A., Kelkar, A., Song, H.-J., Yang, H., and Konsolaki, M. (2004). A model for studying Alzheimer's Abeta42-induced toxicity in Drosophila melanogaster. Mol. Cell. Neurosci. *26*, 365–375.

60. Lodato, M.A., Rodin, R.E., Bohrson, C.L., Coulter, M.E., Barton, A.R., Kwon, M., Sherman, M.A., Vitzthum, C.M., Luquette, L.J., Yandava, C.N., et al. (2018). Aging and neurodegeneration are associated with increased mutations in single human neurons. Science *359*, 555–559.

61. Welch, G.M., Boix, C.A., Schmauch, E., Davila-Velderrain, J., Victor, M.B., Dileep, V., Bozzelli, P.L., Su, Q., Cheng, J.D., Lee, A., et al. (2022). Neurons burdened by DNA double-strand breaks incite microglia activation through antiviral-like signaling in neurodegeneration. Sci. Adv *8*, 4662.

62. Welch, G., and Tsai, L. (2022). Mechanisms of DNA damage-mediated neurotoxicity in neurodegenerative disease. EMBO Rep *23*, 54217.

63. Mesulam, M., Shaw, P., Mash, D., and Weintraub, S. (2004). Cholinergic nucleus basalis tauopathy emerges early in the aging-MCI-AD continuum. Ann. Neurol *55*, 815–828.

64. Bartus, R.T., Dean, R.L., Beer, B., and Lippa, A.S. (1982). The cholinergic hypothesis of geriatric memory dysfunction. Science *217*, 408–414. 10.1126/science.7046051.

65. Grundke-Iqbal, I., Iqbal, K., Quinlan, M., Tung, Y.C., Zaidi, M.S., and Wisniewski, H.M. (1986). Microtubule-associated protein tau. A component of Alzheimer paired helical filaments. J. Biol. Chem *261*, 6084–6089.

66. Lee, V.M., Balin, B.J., Otvos, L., and Trojanowski, J.Q. (1991). A68: a major subunit of paired helical filaments and derivatized forms of normal Tau. Science *251*, 675–678. 10.1126/science.1899488.

67. Kamenetz, F., Tomita, T., Hsieh, H., Seabrook, G., Borchelt, D., Iwatsubo, T., Sisodia, S., and Malinow, R. (2003). APP processing and synaptic function. Neuron *37*, 925–937.

68. Strittmatter, W.J., Saudners, A.M., Schmechel, D., Pericak-Vance, M., Enghild, J., Salvesen, G.S., and Roses, A.D. (1993). Apolipoprotein E: high-avidity binding to beta-amyloid and increased frequency of type 4 allele in late-onset familial Alzheimer disease. Proc. Natl. Acad. Sci. U.S.A *90*, 1977–1981.

69. Corder, E.H., Saunders, A.M., Strittmatter, W.J., Schmechel, D.E., Gaskell, P.C., Small, G.W., Roses, A.D., Haines, J.L., and Pericak-Vance, M.A. (1993). Gene dose of apolipoprotein E type 4 allele and the risk of Alzheimer's disease in late onset families. Science *261*, 921–923.

70. Shulman, J.M., Imboywa, S., Giagtzoglou, N., Powers, M.P., Hu, Y., Devenport, D., Chipendo, P., and Chibnik Functional screening in Drosophila identifies Alzheimer's disease susceptibility genes and implicates Tau-mediated mechanisms. Hum. Mol. Genet *23*, 870–877.

71. Blass, J., and Gibson, G. (1991). The role of oxidative abnormalities in the pathophysiology of Alzheimer's disease. Revue Neurologique *147*, 513–525.

72. Wong-Riley, M., Antuono, P., Ho, K.-C., Egan, R., Hevner, R., Liebl, W., Huang, Z., Rachel, R., and Jones, J. (1997). Cytochrome oxidase in Alzheimer's disease: biochemical, histochemical, and immunohistochemical analyses of the visual and other systems. Vision Res *36*, 3593–3608.

73. David, D.C., Hauptmann, S., Scherping, I., Schuessel, K., Keil, U., Rizzu, P., Ravid, R., Druose, S., Brandt, U., Müller, W.E., et al. (2005). Proteomic and functional analyses reveal a mitochondrial dysfunction in P301L tau transgenic mice. J. Biol. Chem *280*, 23802–23814.

74. DuBoff, B., Götz, J., and Feany, M.B. (2012). Tau promotes neurodegeneration via DRP1 mislocalization in vivo. Neuron *75*, 618–632.

75. DuBoff, B., Feany, M., and Götz, J. (2013). Why size matters – balancing mitochondrial dynamics in Alzheimer's disease. Trends in Neurosci *36*, 325–335.

76. Frost, B., Götz, J., and Feany, M.B. (2015). Connecting the dots between tau dysfunction and neurodegeneration. Trends Cell Biol *25*, 46–53.

77. Miller, M.B., Huang, A.Y., Kim, J., Zhou, Z., Kirkham, S.L., Maury, E.A., Ziegenfuss, J.S., Reed, H.C., Neil, J.E., Rento, L., et al. (2022). Somatic genomic changes in single Alzheimer's disease neurons. Nature *604*, 714–722.

78. Dileep, V., Boix, C.A., Mathys, H., Marco, A., Welch, G.M., Meharena, H.S., Loon, A., Jeloka, R., Peng, Z., Bennett, D.A., et al. (2023). Neuronal DNA double-strand breaks lead to genome structural variations and 3D genome disruption in neurodegeneration. Cell *186*, 4404–4421.

79. Mathys, H., Peng, Z., Boix, C.A., Victor, M.B., Leary, N., Babu, S., Abdelhady, G., Jiang, X., Ng, A.P., Ghafari, K., et al. (2023). Single-cell atlas reveals correlates of high cognitive function, dementia, and resilience to Alzheimer's disease pathology. Cell *186*, 4365–4385.

80. Khurana, V., Lu, Y., Steinhilb, M.L., Oldham, S., Shulman, J.M., and Feany, M.B. (2006). TOR-mediated cell-cycle activation causes neurodegeneration in a Drosophila tauopathy model. Curr. Biol *16*, 230–241.

81. Kubben, F.J., Peeters-Haesevoets, A., Engels, L.G., Baeten, C.G., Schutte, B., Arends, J.W., Stockbrügger, R.W., and Blijham, G.H. (1994). Proliferating cell nuclear antigen (PCNA): a new marker to study human colonic cell proliferation. Gut *35*, 530–535.

82. Curtis, M.A., Penney, E.B., Pearson, A.G., van Roon-Mom, W.M.C., Butterworth, N.J., Dragunow, M., Connor, B., and Faull, R.L.M. (2003). Increased cell proliferation and neurogenesis in the adult human Huntington's disease brain. Proceedings of the National Academy of Sciences *100*, 9023–9027. 10.1073/pnas.1532244100.

83. Kruman, I.I., Wersto, R.P., Cardozo-Pelaez, F., Smilenov, L., Chan, S.L., Chrest, F.J., Emokpae, R., Gorospe, M., and Mattson, M.P. (2004). Cell cycle activation linked to neuronal cell death initiated by DNA damage. Neuron *41*, 549–561. 10.1016/s0896-6273(04)00017-0.

84. Park, D.S., Levine, B., Ferrari, G., and Greene, L.A. (1997). Cyclin dependent kinase inhibitors and dominant negative cyclin dependent kinase 4 and 6 promote survival of NGF-deprived sympathetic neurons. J. Neurosci *17*, 8975–8983.

85. McShea, A., Lee, H.-G., Petersen, R.B., Casadesus, G., Vincent, I., Linford, N.J., Funk, J.-O., Shapiro, R.A., and Smith, M.A. (2007). Neuronal cell cycle re-entry mediates Alzheimer disease-type changes. Biochim. Biophys. Acta *1772*, 467–472.

86. Khurana, V., Merlo, P., DuBoff, B., Fulga, T.A., Sharp, K.A., Campbell, S.D., Götz, J., and Feany, M.B. (2011). A neuroprotective role for the DNA damage checkpoint in tauopathy. Aging cell *11*, 360–362.

87. Patnaik, D., Pao, P.-C., Zhao, W.-N., Silva, M.C., Hylton, N.K., Chindavong, P.S., Pan, L., Tsai, L.-H., and Haggarty, S.J. (2021). Exifone Is a Potent HDAC1 Activator with Neuroprotective Activity in Human Neuronal Models of Neurodegeneration. ACS Chem. Neurosci. *12*, 271–284. 10.1021/acschemneuro.0c00308.

88. Pao, P.-C., Penney, J., and Tsai, L.-H. (2019). Examining the role of HDACs in DNA double-strand break repair neurons. Methods Mol. Biol, 225–234.

89. Pao, P.-C., Patnaik, D., Watson, L.A., Gao, F., Pan, L., Wang, J., Adaikkan, C., Penney, J., Cam, H.P., Huang, W.-C., et al. (2020). HDAC1 modulates OGG1-initiated oxidative DNA damage repair in the aging brain and Alzheimer's disease. Nat Commun *11*, 2484. 10.1038/s41467-020-16361-y.

90. Woods, J., Snape, M., and Smith, M.A. (2007). The cell cycle hypothesis of Alzheimer's disease: Suggestions for drug development. Biochimica et Biophysica Acta (BBA) - Molecular Basis of Disease *1772*, 503–508. 10.1016/j.bbadis.2006.12.004.

91. Kim, D., and Tsai, L.-H. (2009). Linking Cell Cycle Reentry and DNA Damage in Neurodegeneration. Annals of the New York Academy of Sciences *1170*, 674–679. 10.1111/j.1749-6632.2009.04105.x.

92. Jiang, L., Lin, W., Zhang, C., Ash, P.E.A., Verma, M., Kwan, J., Vilet, E., Yang, Z., Cruz, A.L., Boudeau, S., et al. (2021). Interaction of tau with HNRNPA2B1 and N6-methyladenosine RNA mediates the progression of tauopathy. Mol. Cell *81*, 4209–4227.

93. Haenig, C., Atias, N., Taylor, A.K., Mazza, A., Schaefer, M.H., Russ, J., Riechers, S.-P., Jain, S., Coughlin, M., J-, F., et al. (2020). Interactome mapping provides a network of neurodegenerative disease proteins and uncovers widespread protein aggregation in affected brains. Cell Rep *32*, 1–15.

94. Sonawane, A.R., Platig, J., Fagny, M., Chen, C.-Y., Paulson, J.N., Lopes-Ramos, C.M., DeMeo, D.L., Quackenbush, J., Glass, K., and Kuijjer, M.L. (2017). Understanding Tissue-Specific Gene Regulation. Cell Reports *21*, 1077–1088. 10.1016/j.celrep.2017.10.001.

95. Paulo, J.A., and Gygi, S.P. (2018). Isobaric Tag-Based Protein Profiling of a Nicotine-Treated Alpha7. Proteomics *18*, e1700475.

96. McAlister, G.C., Nusinow, D.P., Jedrychowski, M.P., Wühr, M., Huttlin, E.L., Erickson, B.K., Rad, R., and Haas (2014). MultiNotch MS3 enables accurate, sensitive, and multiplexed detection of differential expression across cancer cell line proteomes. Anal. Chem *86*.

97. Avanesov, A.S., Ma, S., Pierce, K.A., Yim, S.H., Lee, B.C., Clish, C.B., and Gladyshev, V.N. (2014). Age- and diet-associated metabolome remodeling characterizes the aging process driven by damage accumulation. Elife *3*, e02077.

98. Kuleshov, M.V., Jones, M.R., Rouillard, A.D., Fernandez, N.F., Duan, Q., Wang, Z., Koplev, S., Jenkins, S.L., Jagodnik, K.M., Lachmann, A., et al. (2016). Enrichr: a comprehensive gene set enrichment analysis web server 2016 update. Nucleic Acids Res *8*, 90–97.

99. Raudvere, U., Kolberg, L., Kuzmin, I., Arak, T., Adler, P., Peterson, H., and Vilo, J. (2019). g:Profiler: a web server for functional enrichment analysis and conversions of gene lists (2019 update). Nucleic Acids Res *47*, 191–198.

100. Pirhaji, L., Milani, P., Leidl, M., T, Avila-Pacheco, J., Clish, C.B., White, F.M., Saghatelian, A., and Fraenkel, E. (2016). Revealing disease-associated pathways by network integration of untargeted metabolomics. Nat. Methods *12*, 770–776.

101. Bennett, D.A., Buchman, A.S., Boyle, P.A., Barnes, L.L., Wilson, R.S., and Schneider, J.A. (2018). Religious Orders Study and Rush Memory and Aging Project. J Alzheimers Dis *64*, S161–S189. 10.3233/JAD-179939.

102. Mostafavi, S., Gaiteri, C., Sullivan, S.E., White, C.C., Tasaki, S., Xu, J., Taga, M., Klein, H.-U., Patrick, E., Komashko, V., et al. (2018). A molecular network of the aging human brain provides insights into the pathology and cognitive decline of Alzheimer's disease. Nat Neurosci *21*, 811–819. 10.1038/s41593-018-0154-9.

103. Chibnik, L.B., White, C.C., Mukherjee, S., Raj, T., Yu, L., Larson, E.B., Montine, T.J., Keene, C.D., Sonnen, J., Schneider, J.A., et al. (2018). Susceptibility to neurofibrillary tangles: role of the PTPRD locus and limited pleiotropy with other neuropathologies. Mol Psychiatry *23*, 1521–1529. 10.1038/mp.2017.20.

104. Wang, M., Beckmann, N.D., Roussos, P., Wang, E., Zhou, X., Wang, Q., Ming, C., Neff, R., Ma, W., Fullard, J.F., et al. (2018). The Mount Sinai cohort of large-scale genomic, transcriptomic and proteomic data in Alzheimer's disease. Sci Data *5*, 180185. 10.1038/sdata.2018.185.

105. Allen, M., Carrasquillo, M.M., Funk, C., Heavner, B.D., Zou, F., Younkin, C.S., Burgess, J.D., Chai, H.-S., Crook, J., Eddy, J.A., et al. (2016). Human whole genome genotype and transcriptome data for Alzheimer's and other neurodegenerative diseases. Sci Data *3*, 160089. 10.1038/sdata.2016.89.

106. Fromer, M., Roussos, P., Sieberts, S.K., Johnson, J.S., Kavanagh, D.H., Perumal, T.M., Ruderfer, D.M., Oh, E.C., Topol, A., Shah, H.R., et al. (2016). Gene expression elucidates functional impact of polygenic risk for schizophrenia. Nat Neurosci *19*, 1442–1453. 10.1038/nn.4399.

107. Zhang, B., Gaiteri, C., Bodea, L.-G., Wang, Z., McElwee, J., Podtelezhnikov, A.A., Zhang, C., Xie, T., Tran, L., Dobrin, R., et al. (2013). Integrated systems approach identifies genetic nodes and networks in late-onset Alzheimer's disease. Cell *153*, 707–720. 10.1016/j.cell.2013.03.030.

108. Ramasamy, A., Trabzuni, D., Guelfi, S., Varghese, V., Smith, C., Walker, R., De, T., Coin, L., de Silva, R., Cookson, M.R., et al. (2014). Genetic variability in the regulation of gene expression in ten regions of the human brain. Nat Neurosci *17*, 1418–1428. 10.1038/nn.3801.

109. Lonsdale, J., Thomas, J., Salvatore, M., Phillips, R., Lo, E., Shad, S., Hasz, R., Walters, G., Garcia, F., Young, N., et al. (2013). The Genotype-Tissue Expression (GTEx) project. Nat Genet *45*, 580–585. 10.1038/ng.2653.

110. A.C.'t Hoen P., Friedländer M.R., Almlöf J., Sammeth M., Pulyakhina I., Anvar S.Y., Laros J.F.J., Buermans H.P.J., Karlberg O., and Brännvall M. (2013). Reproducibility of High-Throughput MRNA and Small RNA Sequencing across Laboratories. Nat. Biotech *31*, 1015–1022.

111. Patterson, N., Price, A.L., and Reich, D. (2006). Population Structure and Eigenanalysis. PLoS Genet *2*, 190.

112. Buhm, H., and Eskin, E. (2011). Random-Effects Model Aimed at Discovering Associations in Meta- Analysis of Genome-Wide Association Studies. Am. J. Hum. Genet *88*, 586–598.

113. Grant, C.E., Bailey, T.L., and Noble, W.S. (2011). FIMO: scanning for occurrences of a given motif. Bioinformatics *27*, 1017–1018.

114. Pourhaghighi, R., Ash, P.E.A., Phanse, S., Goebels, F., Hu, L.Z.M., Chen, S., Zhang, Y., Wierbowski, S.D., Boudeau, S., Moutaoufik, M.T., et al. (2020). BraInMap Elucidates the Macromolecular Connectivity Landscape of Mammalian Brain. Cell Syst *10*, 333-350.e14. 10.1016/j.cels.2020.03.003.

115. Drummond, E., Pires, G., MacMurray, C., Askenazi, M., Nayak, S., Bourdon, M., Safar, J., Ueberheide, B., and Wisniewski, T. (2020). Phosphorylated tau interactome in the human Alzheimer's disease brain. Brain *143*, 2803–2817. 10.1093/brain/awaa223.

116. Villaveces, J.M., Jiménez, R.C., Porras, P., Del-Toro, N., Duesbury, M., Dumousseau, M., Orchard, S., Choi, H., Ping, P., Zong, N.C., et al. (2015). Merging and scoring molecular interactions utilizing existin community standards: tools, use-cases and a case study. Database, 131.

117. Hu, Y., Flockhart, I., Vinayagam, A., Bergwitz, C., Berger, B., Perrimon, N., and Mohr, S.E. (2011). An integrative approach to ortholog prediction for disease-focused and other functional studies. BMC Bioinformatics *12*, 357.

118. Hu, Y., Sopko, R., Chung, V., Foos, M., Studer, R.A., Landry, S.D., Liu, D., Rabinow, L., Gnad, F., Beltrao, P., et al. (2019). iProteinDB: An Integrative Database of Drosophila Post-translational Modifications. G3 *9*, 1–11.

119. Gyori, B.M., Venkatachalam, G., Thiagarajan, P.S., Hsu, D., and Clement, M.-V. (2014). OpenComet: an automated tool for comet assay image analysis. Redox Biol *2*, 457–465.

120. Nehme, R., Zuccaro, E., Ghosh, S.D., Li, C., Sherwood, J.L., Pietilainen, O., Barrett, L.E., Limone, F., Worringer, K.A., Kommineni, S., et al. (2018). Combining NGN2 Programming with Developmental Patterning Generates Human Excitatory Neurons with NMDAR-Mediated Synaptic Transmission. Cell Rep *23*, 2509–2523. 10.1016/j.celrep.2018.04.066.

121. Zirin, J., Hu, Y., Liu, L., Yang-Zhou, D., Colbeth, R., Yan, D., Ewen-Campen, B., Tao, R., Vogt, E., VanNest, S., et al. (2020). Large-Scale Transgenic Drosophila Resource Collections for Loss- and Gain-of-Function Studies. Genetics *214*, 755–767. 10.1534/genetics.119.302964.